Biomarker Research

RESEARCH Open Access

Precision oncology in a dish: patient-derived glioma organoids to guide novel therapeutic strategies

Alvaro Monago-Sánchez[1,2], Laura Mateos-Madrigal[1,2], Josefa Carrión-Navarro[1,2], Ana Hernández-Martínez[1,2], Carlos Martínez-Riveiro[1,2], María Castelló-Pons[3,4], María Victoria Pacheco-Fuenmayor[1,2], Raquel Gutiérrez-González[5,6], Noemí Lomillos-Prieto[5], Ricardo Prat-Acín[7], Santiago Gil-Robles Mathieu[8], Cristina Aracil-González[8], Angel Pérez-Núñez[9,10], Francisco Pérez-Rodríguez[11,12], Pilar Sánchez-Gómez[3], Beatriz Martín-Jouve[13], Antonio J. Sánchez-López[14,15], Noemi García-Romero[1*] and Ángel Ayuso-Sacido[1,2,16,17*]

Abstract

Background Gliomas are the most common primary brain tumors in adults and encompass a spectrum from IDH-mutant gliomas to highly aggressive IDH-wild type glioblastomas (GBM). Despite advances in our understanding of glioma biology, GBM remains largely incurable, with a median overall survival (mOS) of approximately 15 months and minimal improvements over recent decades. The current standard of care, maximal surgical resection followed by radiotherapy and temozolomide (TMZ) chemotherapy, has proven insufficient, and experimental approaches such as immune checkpoint inhibitors and CAR-T cell therapies have also failed to provide meaningful survival benefits. These limitations highlight the urgent need for innovative, patient-specific platforms to evaluate novel therapeutic strategies.

Methods In this study, we established patient-derived glioma organoids (GOs) from 61 patients, including both IDH-mutant gliomas (GOmut) and IDH-wild type glioblastoma (GOwt). These organoids were characterized by a variety of techniques against their parental tumors. Afterwards, we performed *in silico* drug discovery with paired RNA-seq data and validated the results with diverse glioma models.

Results GOs recapitulated the cellular heterogeneity, histological architecture, and molecular signatures of their parental tumors, including the preservation of clinically relevant features such as immune profiles, vascular structures, and tumor subtype. Notably, GOmuts retained the IDH mutation over extended culture periods. Importantly, GOs maintained resistance to standard chemotherapeutic agents, mirroring the limited response of gliomas to conventional chemotherapy. Our unbiased *in silico* screening via the DiSCoVER platform applied to RNA-seq data from paired tumors and GOs identified alectinib, dabrafenib, and ruxolitinib as promising candidates. All three compounds

*Correspondence:
Noemi García-Romero
noemi.garcia@ufv.es
Ángel Ayuso-Sacido
angel.ayuso@isciii.es

Full list of author information is available at the end of the article

proved effective in in vitro cytotoxicity assays, with alectinib and ruxolitinib displaying significant antitumoral effects in vitro.

Conclusions Our findings establish GOs as a clinically relevant and biologically faithful platform for therapeutic screening in glioma. By integrating transcriptomics-based drug discovery with a patient-specific organoid model, we present an easy to implement platform for more effective and personalized treatments for glioma patients. Our findings also support the inclusion of two compounds, alectinib and ruxolitinib, in future clinical investigations.

Keywords Glioma, Glioblastoma, Organoids, Personalized therapies

Background

Malignant gliomas are classified based on their histological characteristics and the presence or absence of isocitrate dehydrogenase (IDH) mutation into IDH-mutant gliomas and IDH-wild type glioblastoma (GBM). GBM is the most prevalent and aggressive form, with an incidence of 3.22 cases per 100,000 people [1]. GBM is further marked by significant inter- and intra-tumoral heterogeneity [2] contributing to its poor prognosis, with a median overall survival (mOS) of only 15 months and a 5-year survival rate of around 5% [3]. Despite these challenges, the standard of care (SOC) therapy, comprising maximal surgical resection followed by radiotherapy with concomitant and adjuvant temozolomide (TMZ) chemotherapy, has remained largely unchanged for decades, with limited improvements in patient outcomes [4, 5]. On the other hand, studying IDH-mutant gliomas presents additional challenges due to their lower proliferation rates and heterogeneity. Moreover, traditional models fail to maintain the clinically relevant IDH mutation, which hinders the development of conventional preclinical models such as established cell line cultures [6, 7].

The urgent need for new therapeutic approaches is underscored by the persistent failure of current treatments to significantly improve survival outcomes for glioma patients. Despite decades of research, GBM remains a largely incurable disease, with standard therapies offering only marginal benefits. Moreover, alternative experimental strategies such as immune checkpoint inhibitors and CAR-T cell therapies have also failed to yield meaningful clinical success in this context [8, 9]. These challenges highlight the need for the development of innovative, patient-specific strategies to identify effective therapeutic options. Given the variability in tumor characteristics, tumor-derived preclinical models present an opportunity to screen novel pharmaceutical options in a personalized, patient-specific manner, especially in incurable malignancies like gliomas [10]. In this context, patient-derived organoids have emerged as a highly promising tool. Unlike traditional 2D cultures, glioma organoids retain key features of the original tumor, including cellular diversity, tissue architecture, and the tumor microenvironment. These characteristics allow them to more accurately replicate patient-specific drug responses, making them ideal platforms for therapeutic screening and disease modeling [11, 12]. Additionally, organoids are faster to establish and more cost-effective to maintain than animal-based patient-derived xenografts (PDX) [13]

In this study, we generated malignant glioma-derived organoids (GOs) from 61 patients, encompassing both IDH-mutant (GOmut) and GBM (GOwt), to identify novel therapeutic options. GOs were used to evaluate responses to standard chemotherapeutic agents commonly used in glioma treatment, like TMZ, which proved to be ineffective, mirroring the clinical relapse of the original patients. Additionally, we employed the DiSCoVER platform, an RNA-seq-based tool that predicts drug sensitivity by contrasting tumor gene expression data with three reference databases (CTRP, CCLE, and GDSC), which contain drug response profiles for over 600 compounds [14–17], to perform an unguided and unbiased *in silico* drug screening, which identified 3 promising compounds; alectinib, ruxolitinib and dabrafenib. These candidates were subsequently validated in a prospective GOwt cohort, glioma stem-like cells (GSCs), glioma cell lines, and both a classical (U87) and a novel GO xenograft model, confirming their antitumoral activity across multiple glioma models.

Altogether, our work highlights the potential of GOs as predictive, patient-specific models that preserve the intricate biological features of malignant gliomas. By combining high-fidelity *in vitro* systems with advanced bioinformatics, this approach not only enhances our understanding of glioma biology but also sets the groundwork for their integration into clinical decision-making pipelines, potentially informing therapeutic choices, guiding clinical trial design, and ultimately contributing to improved patient outcomes.

Methods

Human samples

Tumor specimens and peripheral blood samples were obtained from patients undergoing surgery at Hospital Universitario Puerta de Hierro (Madrid, Spain) via its biobank, as well as from Hospital Universitario Quironsalud Madrid (Madrid, Spain) and Hospital Universitario

12 de Octubre (Madrid, Spain) immediately following resection.

GOs generation, culture, and biobanking

GOs were generated, maintained, biobanked and recovered based on a previously described protocol [18, 19], with the only modification being the absence of agitation. GOs were cultured with M-GO, containing DMEM/F12, Neurobasal, non-essential amino acids, GlutaMAX supplement, N2 supplement, B27 Supplement, Penicillin-Streptomycin, 2-Mercaptoethanol and human insulin (all provided by GIBCO, USA). GOs were tested routinely for mycoplasma.

Tissue processing for downstream applications

Tumor samples and GOs were collected, washed in 1X PBS, and fixed in 4% paraformaldehyde (PFA) overnight under constant agitation. Samples designated for hematoxylin and eosin (H&E) staining were stored in 70% ethanol at 4 °C until further processing. Samples intended for immunofluorescence (IF) and immunohistochemistry (IHC) were embedded in optimal cutting temperature compound, snap-frozen in cryomolds, and stored at −80 °C.

Cryostat sectioning was performed to obtain 10 µm sections from the frozen samples, which were then mounted on poly-lysine-coated glass slides by the Histology Unit at San Pablo CEU IMMA (Madrid, Spain).

Hematoxylin and eosin (H&E) staining and imaging

Tissue dehydration and paraffin embedding were performed manually by the Histology Unit at San Pablo CEU IMMA (Madrid, Spain). Standard H&E staining was conducted on 5 µm sections. Slides were imaged using a Leica Aperio VERSA pathology scanner equipped with a 20x objective.

Immunofluorescence (IF) and immunohistochemistry (IHC) staining and image acquisition

Tissue sections were washed, permeabilized with 0.1% Triton-X, and incubated in a 10% blocking solution of specific serum for 1 hour. Sections were incubated overnight at 4º C with primary antibodies (Supplementary Table 1) and washed. Then, for IF staining, tissues were incubated with Alexa Fluor-conjugated secondary antibodies for 1 hour at room temperature (RT) (Supplementary Table 2). Sections were subsequently counterstained with DAPI. All fluorescence images were captured using the Leica Thunder Imager system with a 20x apochromatic objective. Raw images were processed with the Thunder deconvolution function in Leica LAS X software and assembled using Fiji software version 2.3.0.

For IHC staining, tissues were incubated with a biotinylated secondary antibody (Supplementary Table 2) for 1 hour at RT. After washing, sections were treated with the VECTASTAIN® Elite® ABC Kit (Vector Laboratories, USA), developed with DAB, and counterstained with hematoxylin. Coverslips were mounted with Eukitt® quick hardening mounting medium following dehydration. Brightfield images were acquired with a Leica Aperio VERSA pathology scanner.

Periodic acid-schiff (PAS) staining

FFPE GOs were subjected to standard IHC protocols. Before counterstaining, slides were washed and standard PAS staining was performed using the Periodic Acid-Schiff Kit (epredia, USA) following the manufacturer's protocol. Brightfield images were acquired with a Leica Aperio VERSA pathology scanner.

Bromodeoxyuridine (BrdU) staining

GOs were incubated overnight in M-GO medium containing 20 µM BrdU. Following incubation, GOs were collected, washed, and processed according to the IF staining protocol described above.

GO growth measurement

GOs were seeded in 6-well ultra-low attachment plates at varying densities: low (10 GOs per well), medium (20 GOs per well), and high (40 GOs per well) immediately after establishment. Media was refreshed every 48 hours, and widefield images were captured weekly using a Motic binocular stereomicroscope (Motic, China). Diameters were measured in Fiji software (version 2.3.0) by recording two perpendicular diameters per GO; the average of these measurements was then compared to the baseline diameter average recorded at week 0.

Quantitative real time PCR (qRT-PCR) of tissue and GOs

Fragments of tissue and paired GOs were dissociated, and total RNA was extracted using the RNeasy Mini Kit (Qiagen, Germany) according to the manufacturer's instructions. One microgram of purified RNA was used for complementary DNA (cDNA) synthesis with the High-Capacity cDNA Reverse Transcription Kit (Applied Biosystems, USA). Quantitative real time PCR (qRT-PCR) was conducted in an optical 96-well plate using a Bio-Rad CFX Connect Real-Time PCR system. SYBR Green dye (Takara Bio USA, Inc.) was used for detection. Gene expression levels were analyzed with specific primers (Supplementary Table 3), and *β-actin* was used as a reference gene for normalization.

Droplet digital PCR (ddPCR)

DNA was extracted from GOs and liquid biopsy samples using the DNeasy Blood & Tissue Kit (Qiagen, Germany) according to the manufacturer's protocol. Droplets were generated with the Q×200 Droplet Generator (Bio-Rad,

Spain) using DNA at a concentration of 10 ng/µL (quantified by Nanodrop) per sample, combined with ddPCR Droplet Reader Oil (Bio-Rad, Spain). Plates were sealed with the P×1 PCR Plate Sealer (Bio-Rad, Spain), and amplification was performed using the C100 Touch Thermal Cycler (Bio-Rad, Spain) with ddPCR Supermix (Bio-Rad, Spain) and the ddPCR Mutation Assay IDH1 R132H probe (Bio-Rad, Spain). Droplet reading was conducted with the Q×200 Droplet Reader (Bio-Rad, Spain), and data analysis was performed using QuantaSoft™ software version 1.7.

D-2-Hydroxyglutarate (D-2HG) measurement

The concentration of D-2HG in GOs and their corresponding culture media was quantified using the PicoProbe D-2-Hydroxyglutarate (D2HG) Assay Kit (BioVision, USA). Frozen samples were thawed, homogenized, and centrifuged at 10,000 × g for 5 minutes at 4 °C to remove cellular debris. The resulting supernatants were then processed according to the manufacturer's instructions.

Sanger sequencing of *IDH1* G395A

Genomic DNA was extracted from GOs using the DNeasy Blood & Tissue Kit (Qiagen, Germany) according to the manufacturer's instructions. The extracted DNA was amplified by conventional PCR using the following primers: forward, CGGTCTTCAGAGAAGCCATT; reverse, GCAAAATCACATTATTGCCAAC. PCR products were purified, and standard Sanger sequencing was performed by the Genomics Service at the Instituto de Investigaciones Biomédicas Sols-Morreale (IIBM, Madrid, Spain). Resulting sequences were aligned and compared using the BLAST algorithm. Chromatograms were inspected with FinchTV (version 1.4.0).

Flow cytometry (FC)

Tissue fragments and GOs were dissociated into single-cell suspensions using a combination of mechanical dissociation and the Neural Tissue Dissociation Kit (Miltenyi Biotec, Germany). Cell suspensions were rinsed with 1X PBS, centrifuged, passed through a 70 µm strainer, washed again, and incubated with specific antibodies (Supplementary Table 4). After antibody staining, cells were washed with 1X PBS, and dead cell exclusion was performed using either propidium iodide (Sigma-Aldrich, USA) or Viobility 488 (Miltenyi Biotec, Germany).

Flow cytometric analysis was conducted on a Miltenyi MACSQuant 10 flow cytometer. Results were analyzed using FlowJo software, version 10, with non-labeled controls, compensation controls, and fluorescence minus one controls included.

Transmission electron microscopy (TEM)

Tissue fragments (1 mm^3) and GOs were fixed overnight at 4 °C in a solution containing 2% PFA and 2.5% glutaraldehyde. Samples were washed with phosphate buffered saline (1X PBS), post-fixed (1 h, 4°C) with 1% osmium tetroxide (TAAB Laboratories) in potassium ferricyanide 0.8% (Sigma) and incubated with 2% aqueous uranyl acetate (Electron Microscopy Sciences) for 1 h at 4 °C. Subsequently, samples were dehydrated with increasing concentrations of acetone (anhydrous, VWR) and embedded in epoxy resin TAAB 812 (TAAB Laboratories). Polymerization was carried out for 2 days, 60 °C. Resin blocks were trimmed and ultrathin 70 nm-thick sections were obtained with the UC6 ultramicrotome (Leica Microsystems), transferred to 200 mesh nickel grids (Gilder) and stained with saturated aqueous uranyl acetate (25 min) and lead citrate 0.2% (1 min) at room temperature. Sections were visualised on a JEOL JEM 1400 Flash electron microscope (operating at 100 kV). Micrographs were taken with a Gatan One View digital camera at various magnifications.

Assessment of chemotherapeutic compounds in GOwts

To evaluate GO responses to standard chemotherapeutics, 20 GOs per condition were incubated for 48 hours with either TMZ (250 µM), irinotecan (250 µM), vincristine (10 µM), gefitinib (25 µM), etoposide (5 µM),doxorubicin (0.2 µM), dabrafenib (100 µM), ruxolitinib (120 µM) or alectinib (50 µM) each dissolved in M-GO medium. Dosage was selected based on the average IC50 values of the selected compounds in glioma cell lines from the Genomics of Drug Sensitivity in Cancer database [16].

After 48 hours, GO viability was assessed using the MTS assay. Selected GOs were then processed for H&E staining, IF staining for GFAP and Vimentin, and IHC for γH2AX.

RNA extraction, RNA sequencing and analysis

For RNA sequencing (RNA-seq), GOwts or tissues were collected, rinsed with 1X PBS, and stored in RNAlater at −80 °C. RNA was extracted. and RNA concentration was measured with a Nanodrop spectrophotometer. RNA integrity was assessed using a Bioanalyzer (Agilent Technologies, Spain), with only samples exceeding a RIN value of 7 used for sequencing.

Sequencing was carried out on the DNBSEQ™ platform (BGI TECH SOLUTIONS, Poland) with 150 bp paired-end reads and a sequencing depth of 20 million clean reads per sample, sufficient for downstream differential gene expression analysis.

RNA-seq data analysis was performed with the Dr. Tom bioinformatics platform from BGI. To assess the statistical significance of clustering patterns in heatmaps,

we used a multiscale bootstrap resampling approach implemented in the *pvclust* R package [20]. Clustering was performed using Pearson correlation distance (1 – r) and average linkage, consistent with the metrics used to generate the heatmaps. The resulting Approximately Unbiased (AU) p-values provide a robust and statistically validated measure of cluster reliability, as it estimates the probability that a given cluster is supported by the data beyond random chance. Clusters with AU ≥ 95% were considered statistically significant ($p < 0.05$).

Samples subtype classification

GBM molecular subtypes were assigned using the GlioVis application [21], which integrates three complementary classification algorithms: support vector machines (SVM), k-nearest neighbors (k-NN), and gene set enrichment analysis (GSEA). Each sample received an individual prediction from each method, and a consensus subtype was assigned when at least two of the three classifiers agreed.

Single-cell RNA-seq analysis (scRNA-seq)

scRNA-seq datasets were downloaded from GEO (GSE117891) [22] and GBmap [23]. All analyses were conducted in R (v4.4.1) using the Seurat package (v5.3.0) [24].

After merging raw matrices, cells with < 1 000 UMIs, < 250 genes, or > 15% mitochondrial reads were discarded. Mitochondrial, ribosomal (RPL/RPS) and hemoglobin genes were removed to reduce technical noise. Doublets (DoubletFinder) [25] and ambient-RNA–contaminated cells (decontX) [26] were excluded; genes expressed in < 1% of cells were filtered out.

Data were log-normalised, the 2,000 most variable genes were selected, and counts were scaled. We computed 30 principal components, corrected patient-specific batch effects with Harmony [27], built a shared-nearest-neighbour graph and applied Louvain clustering; 2-D visualisation used UMAP.

Malignant versus non-malignant cells were identified with SCEVAN [28], which infers large-scale copy-number alterations from transcriptomes. Cells with GBM-typical aneuploidies were labelled "tumor", diploid cells "non-tumor". Broad lineages (tumor-associated macrophages, microglia, glia, vasculature, T cells) were assigned by SingleR [29], label transfer from multiple reference atlases, then harmonized at cluster level by majority rule.

RNA-seq deconvolution

Genes not present across all samples were filtered out, and raw read counts were normalized to counts per million. Deconvolution was performed using CIBERSORTx [30] in R (version 4.4.1) applying a custom signature matrix derived from Couturier et al. [31]. The analysis was conducted with batch correction enabled in S-mode, 100 permutations, and quartile normalization disabled.

MTS viability assay and IC50 determination

To assess viability, six GOs of similar size per condition were selected, washed with 1X PBS, and dissociated using a combination of manual and enzymatic digestion (TrypLE Express, Gibco). Cell suspensions were centrifuged, resuspended, and seeded in 96-well plates in 200 µL of M-GO medium. To determine IC50 of GOs, ten GOs per concentration were collected after 48 h treatment, washed with 1X PBS , dissociated manually and enzymatically (TrypLE Express, Gibco), single cell suspensions were centrifuged, washed and seeded in 96 well plates with 200 µL of M-GO. Cell lines were passaged and seeded at a density of 3000 cells per well in a 96-well plate with 100 µL of their respective growth media. Cells were left overnight and subsequently treated for 48 hours. Afterwards, 30 µL of MTS reagent (Promega Biotech Ibérica, Spain) was added to each well, and plates were incubated at 37 °C in the dark for 2 hours. Absorbance was measured using a TECAN Sunrise microplate reader at 492 and 620 nm. Readings were normalized against the control condition. IC50 values were calculated by fitting a nonlinear variable slope curve in Prism software version 10.

Annexin V/propidium iodide (PI) apoptosis assay

Ten GOs per condition were collected after 48 h treatment, washed with 1X PBS, dissociated in collagenase IV (20 min, 37 °C), filtered through a 70 µm strainer, and resuspended in 100 µL Annexin V Binding Buffer (BioLegend, USA). Samples were stained with 5 µL Annexin V–FITC (BioLegend, USA) and 5 µL PI (Sigma-Aldrich, USA) for 15 min at RT, diluted with 400 µL Binding Buffer, and analyzed immediately on a MACSQuant 10 flow cytometer (Miltenyi, Germany). Unstained and compensation controls were included. Data analysis was performed using Kaluza V2.1.

In silico drug sensitivity screening via DiSCoVER

To assess potential drug sensitivities in our samples, RNA-seq gene expression data was analyzed using the DiSCoVER platform (version 1.1) [17]. Bulk expression data from healthy brain samples from the GTEx portal [32] served as reference datasets. The analysis generated a ranked list of potential drug sensitivities for each organoid and its paired parental tissue. For *de novo* drug discovery, the top 20 predicted candidates from each sample were selected. These results were compared across all samples, resulting in two refined lists containing the top 6 compounds for parental tumor tissues and derived GOwts, respectively. From these lists, the top 3

overlapping compounds were identified and selected for subsequent functional validation studies.

Cell lines culture

The primary glioma stem cell (GSC) line GBM38 was generated and maintained following the protocol previously described [33]. Immortalized GBM cell lines U87, LN229, and U373 were cultured in DMEM/F-12 medium (Gibco, USA) supplemented with 10% FBS (Gibco, USA) and 100 U/mL of penicillin/streptomycin (Gibco, USA). All cell lines were maintained under standard cell culture conditions at 37 °C in a humidified atmosphere with 5% CO_2. All cell lines were routinely tested for mycoplasma.

GOwts transwell migration assays

To evaluate migration capabilities, seven similarly sized GOs were dissociated into single-cell suspensions. The resulting solutions, containing M-GO and their respective treatments, were added to the top chamber of an 8 µm pore transwell insert (Corning, USA) placed in a 24-well plate containing 1 mL of M-GO supplemented with heparin, fibroblast growth factor (FGF), and epidermal growth factor (EGF). The setup was maintained under standard growth conditions for 6 hours.

After incubation, transwells were washed with 1X PBS, fixed in 4% PFA, and stained with 0.1% crystal violet. Transwell membranes were cut from the insert and mounted on a standard microscope slide. Images of migrated cells were captured immediately using a Nikon Eclipse microscope (Nikon, Japan).

GBM cell lines wound healing assay

To assess the migration capabilities of GBM cell lines, 500,000 cells per well were seeded in a 6-well plate (Corning, USA) with 3 mL of DMEM/F-12 medium (Gibco, US) supplemented with 10% FBS (Gibco, US). After overnight incubation to achieve full confluency, a wound was created manually using a 200 µL pipette tip. The wells were gently washed twice with 1× PBS to remove cell debris, and fresh medium containing 10% FBS, 100 U/mL of penicillin/streptomycin and the respective drug concentration was added.

Wound areas were imaged immediately after scratching and again after 24 hours using a Leica Thunder Imager system equipped with a 5× apochromatic objective (Leica, Germany). Wound closure was quantified using an automated image analysis macro [34], to minimize bias introduced by manual region selection.

Mice experiments

For in vivo drug studies, whole GOs or 1×10^6 U87 cells were resuspended in cold liquid Matrigel (Corning, USA) and subcutaneously injected into the flank of athymic nude mice. Mice were anesthetized using 5% isoflurane for induction and maintained at 2% during the procedure.

Tumor growth was monitored daily with caliper measurements. Treatments commenced when tumors reached a volume of approximately 200 mm^3. Mice were treated daily via intraperitoneal injections of vehicle, alectinib (25 mg/kg), ruxolitinib (50 mg/kg) or dabrafenib (20 mg/kg). Mice were euthanized either when tumors reached 1500 mm^3 or when tumor burden became apparent, in accordance with ethical guidelines.

Statistical analysis

All statistical analyses were performed using GraphPad Prism software (version 10). Sample normality was assessed with either the Shapiro-Wilk or Kolmogorov-Smirnov test, depending on sample size. For normally distributed data, comparisons among groups were conducted using ANOVA with Welch's correction, while non-parametric data were analyzed with the Kruskal-Wallis test. Statistical significance was represented as follows: $^{***}p < 0.001$, $^{**}p < 0.01$, $^{*}p < 0.05$. Differences among groups were considered statistically significant at $p < 0.05$.

Results

Efficient generation of patient-derived glioma organoids (GOs)

Our cohort of GOs was derived from 61 patients, including IDH-wild type GBM (termed GOwt) and IDH-mutant (termed GOmut) cases, with the majority corresponding to GBM (Fig. 1A and B). Success in GO generation was confirmed by GOs reaching spherical morphology after 2 weeks in culture (Fig. 1C–F), increase in size and histological similarity confirmed via an independent attending pathologist. We also observed cycling cells shown as BrdU positive cells (Fig. 1G), confirming the macroscopic proliferation observations. Overall, we achieved a robust over 90% success rate in GO generation (Fig. 1B).

Seeding density and size severely impact GO growth rates

To determine the optimal conditions for GO growth, we first assessed the effects of culture density on GO expansion. GO diameters were measured in 9.6 cm^2 wells seeded at low (10 GOs per well), medium (20 GOs per well), and high (40 GOs per well) densities. Growth rates were comparable between medium and high densities, while low-density cultures exhibited significantly reduced growth, suggesting that an optimal seeding density of ~ 2 GOs per cm^2 maximizes growth efficiency. Across all conditions, growth rates declined after four weeks, defining this as a practical experimental timeframe (Fig. 2A).

We next investigated how GO size influences cellular distribution and proliferation. When GOs grew to diameters of ~ 3 mm, vimentin expression became restricted

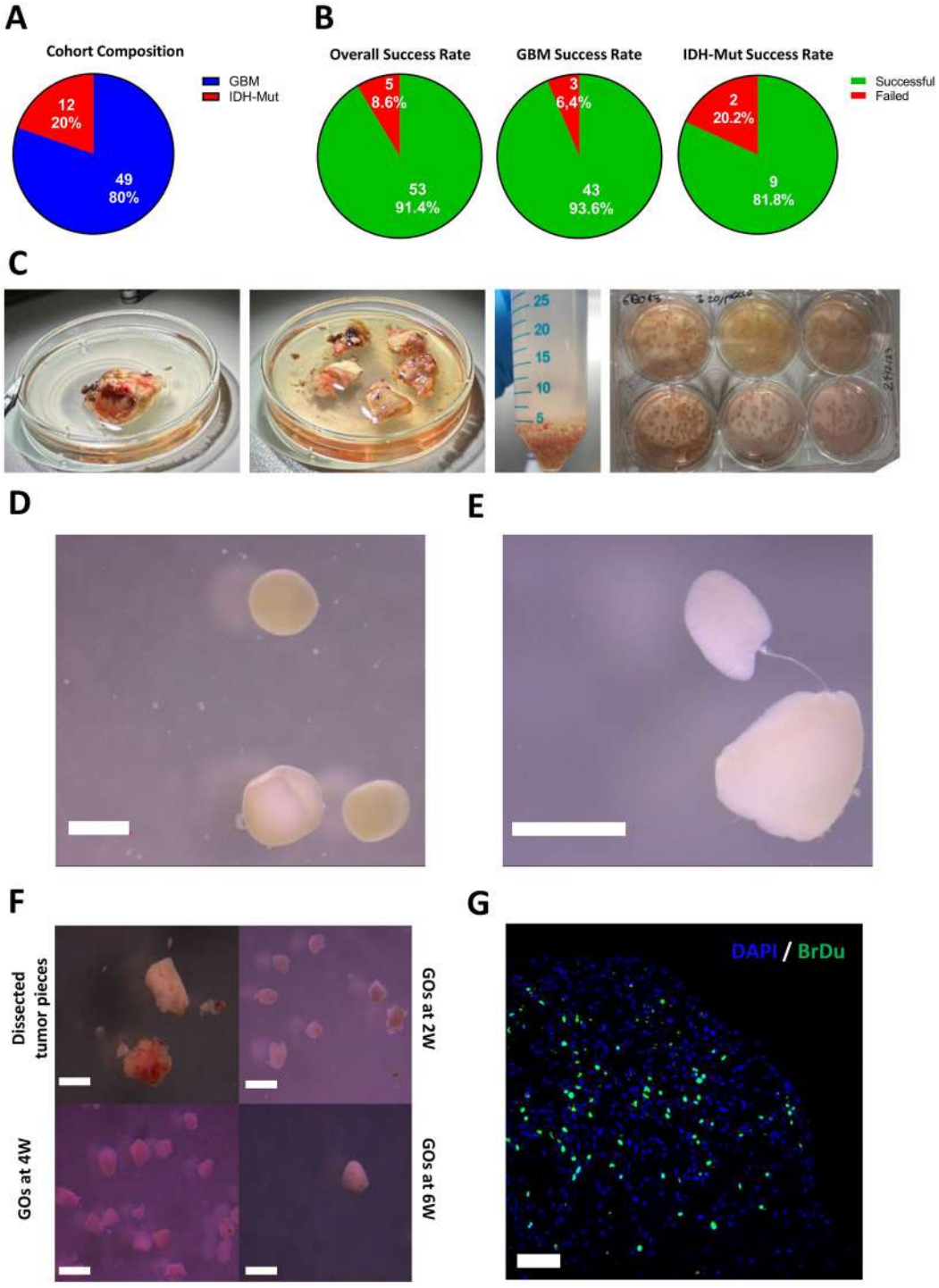

Fig. 1 Generation of patient-derived GOs: (**A**) Sample distribution used for organoid generation, with GBM patients shown in blue, IDH-mutant patients in red. (**B**) GO generation success rates, shown as the number of successful GOs (green) and unsuccessful attempts (red) across all samples (left), GBM samples (center), and IDH-mutant samples (right). (**C**) Images illustrating the organoid generation process, from left to right: original tumor sample, coarse sectioning, final wash of pre-organoids, and seeded pre-organoids. (**D**) Representative brightfield image of fully formed GOs after two weeks in culture. (**E**) Brightfield image showing two organoids in culture connected by a thin tube-like structure. (**F**) Brightfield images depicting organoid progression in culture, from initial tumor dissection to six weeks. Scale bar is 1 mm. (**G**) Immunofluorescence (IF) image of BrdU (green) incorporation in a representative GO, indicating cell proliferation; scale bar = 200 µm

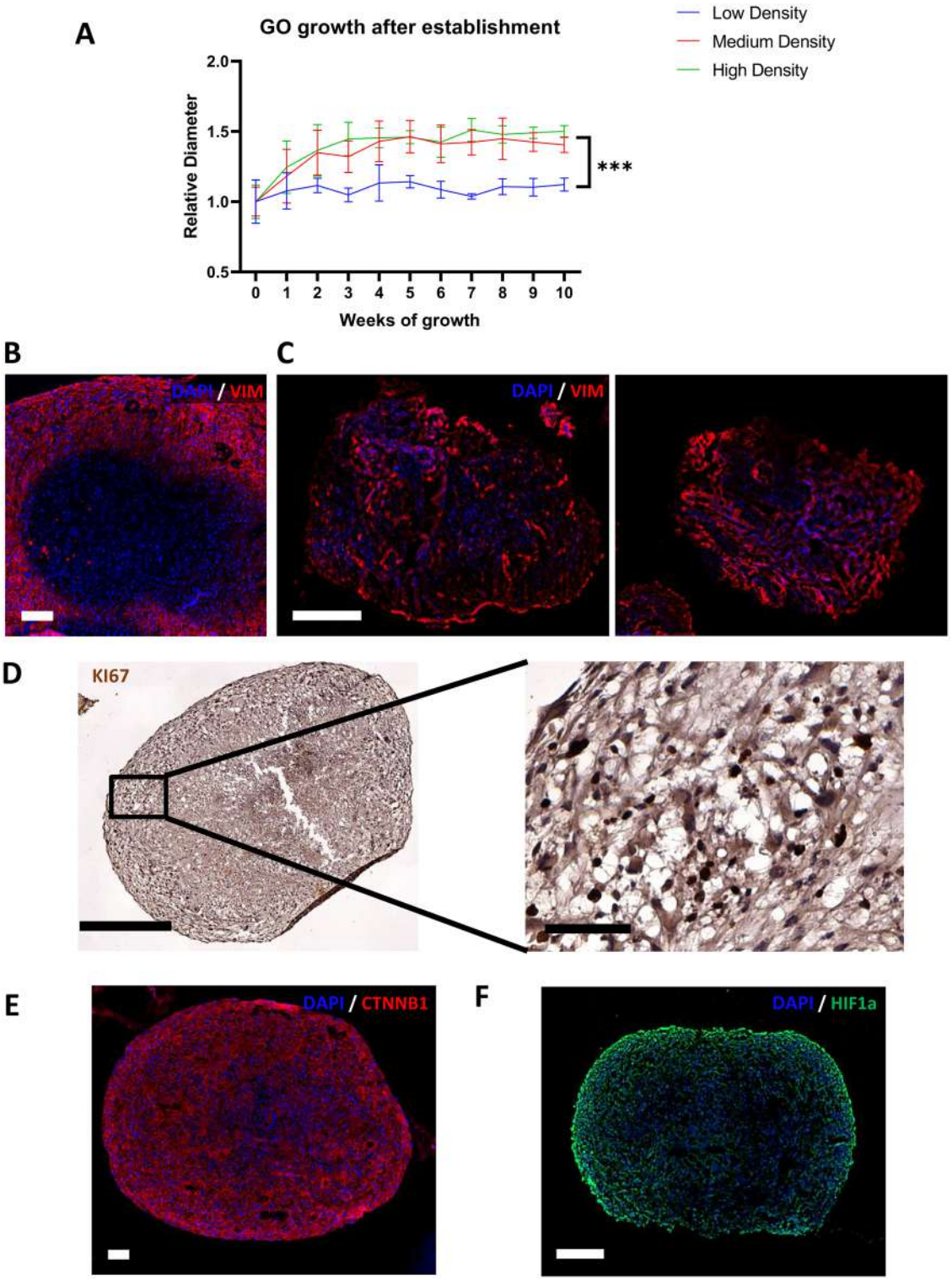

Fig. 2 Effects of seeding density and GO size on growth: (**A**) Relative diameters of a representative GO measured over 10 weeks, with low-density (10 organoids/well), medium-density (20 organoids/well), and high-density (40 organoids/well) culture conditions. Each time point represents the mean diameter, with vertical lines indicating standard deviation (SD). ***$p < 0.0001$. (**B**) IF staining for VIMENTIN (red) in representative GO; scale bar = 200 µm. (**C**) IF staining for VIMENTIN (red) in two different GOs; scale bar = 200 µm. (**D**) IHC staining for Ki67 (dark brown) in GO, with a close-up of the GO periphery (right). Scale bar = 1 mm (left) and 0.1 mm (right). (**E**) IF staining for CTNNB1 (red) in GO; scale bar = 100 µm. (F) IF staining for HIF-1α (green) in a representative GO; scale bar = 200 µm

to the periphery, despite nuclei still being present in the core (Fig. 2B). In contrast, smaller GOs displayed a more homogeneous vimentin distribution (Fig. 2C). A similar core-periphery pattern was observed for Ki-67, indicating that proliferative activity is concentrated in the periphery of larger GOs (Fig. 2D). Interestingly, this pattern was not observed for β-catenin (Fig. 2E) or HIF1α (Fig. 2F), suggesting that oxygen and nutrient diffusion limitations in larger GOs primarily impact proliferation rather than other cellular functions.

Finally, we examined the impact of biobanking on GO growth and histology. While post-biobanked GOs retained their histological characteristics, closely resembling both the original tumor tissue and pre-biobanking GOs (Fig. S1A), they did not increase in size, indicating severely impaired proliferation (Fig. S1B). Next, we wondered whether we could improve the proliferation rates of recovered GOs in an in vivo model. To do so, we selected GOs that had been cryopreserved for longer than 6 months and performed subcutaneous xenografts in athymic mice. We observed that these GOs maintained their original tumorigenic properties (Fig. S1C and D), and we were even able to derive a GSC line from them (Fig. S1E). Together, these findings emphasize that seeding density and GO size significantly influence growth, proliferation, and structural organization. While biobanking preserves histological integrity despite halting proliferation, GOs exceeding 3 mm in diameter develop core-periphery segregation, which may impact their functionality. Maintaining optimal culture conditions is crucial for maximizing GO utility in preclinical studies.

GOs conserve key tumoral histological features and elements of tissular and cellular microarchitecture

To characterize the structure of our GOs, we first performed H&E staining on successfully established GOs. GOwt (Fig. 3A and S1F) and GOmut (Fig. 3B). GOs were evaluated by an independent attending pathologist, who confirmed their resemblance to the original tumor tissue. GOs also displayed diverse tumor cell phenotypes and hallmark glioma features, such as necrotic areas (GO30) and abundant microvasculature (GO8). These histological characteristics remained stable over several weeks and passages in culture (Fig. 3C and S1G).

To further confirm that GOs closely replicate the microstructure of the original tumoral tissue, we examined GOs and their corresponding parental tumors using TEM after two weeks in culture. Initial observations revealed the presence of myelin sheaths in the GOs, consistent with the tissue of origin, although early signs of degeneration were observed (Fig. 3D). We also observed areas of necrosis and edema in both parental tumors and GOs (Fig. 3E), reflecting classic histological features of GBM.

Within the GOs, neurons were readily identified based on nuclear shape and electron density (Fig. 3F). These neurons retained healthy mitochondria (Fig. S2A) and an intact reticulum network, and they also engaged in interactions with nearby cells. This is noteworthy given the challenges of sustaining neurons in vitro [35]. Glial cells were abundant, with close to 25% containing large glycogen deposits (Fig. 3G, S2B, S2C and S2D) and a significant number (50–60%) in both tumors and GOs presented lipid droplets (Fig. 3H, S3A). Oligodendrocytes could be identified close to myelin sheaths (Fig. S3B). Close examination of the cytoplasm of these glial cells showed intact nuclear membranes and well-preserved organelles (Fig. S3C). Cellular projections loaded with ribosomes were observed, suggesting that these are not phagocytic processes (Fig. S3C).

Furthermore, we observed multiple cell-cell interactions, primarily between neurons and glial cells (Fig. 3I and S3D), indicating preserved cellular roles and interactions in the GO model. Tumor cells displayed a range of morphologies and sizes, with healthy mitochondria and enlarged reticulum (Fig. 3J, S3E and S3F). Around 7% of cell projections contained mitochondria, with a density of 5–6 mitochondria per μm^2, consistent with previously described tumor microtube-like structures in gliomas (Fig. S4A and S4B) [36, 37] and matching our macroscopic observations (Fig. 1E). Finally, extracellular matrix (ECM) components, including collagen, were also identified in the GOs (Fig. S4C).

Overall, these findings demonstrate that GOs faithfully replicate the complex histological and ultrastructural features of gliomas, including diverse cellular populations, cell-cell interactions, ECM components, and classical glioma features.

GOs contain heterogeneous cell populations and conserve vascular microstructure

After our general characterization, we decided to focus on their molecular properties. To that end, we began by analyzing protein distribution by IF. We first identified mature astrocytes, differentiated oligodendrocytes and neurons (Fig. 4A and S5). Additionally, we observed the conservation of vascular microarchitecture, including CD31+ structures resembling microvessels and a prominent presence of VEGFA and its receptor VEGFR2 (Fig. 4B). Furthermore, we detected glioma-associated stemness markers CD90, Vimentin, and Nestin (Fig. 4C).

The close resemblance of parental tumors and GOs was confirmed by the expression of stemness markers (Fig. 4D), cell-type markers (Fig. 4E), and vasculature markers (Fig. 4F) Linear regression analysis of these values highlighted a very strong relationship, with R^2 values of 0.79 for GBM and 0.83 for IDH-mutant gliomas (Fig. 4G). Supporting these results, the specific gene expression

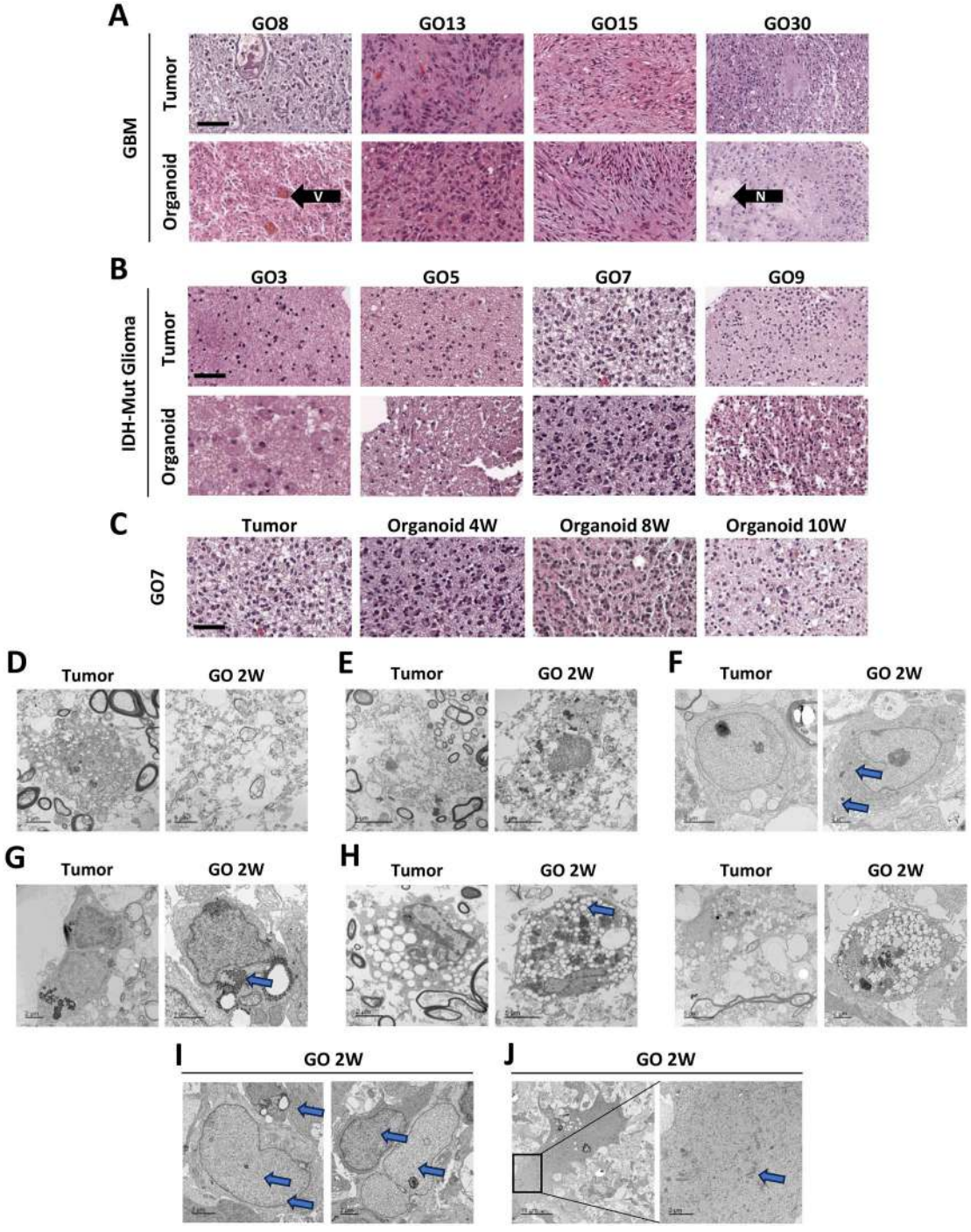

Fig. 3 General characterization of patient-derived GOs: H&E staining of representative sections from original tumor tissue (top) and GOs (bottom) for GBM (**A**) and IDH-mutant glioma (**B**) patients; scale bar = 100 µm. Microvascular areas are marked as "V", while necrotic parts are highlighted with "N" (**C**) Histological progression of a GO in culture, with H&E-stained sections of the original tumor tissue (left) and corresponding GO after several weeks in culture; scale bar = 100 µm. TEM images of: (**D**) Myelin sheaths observed in the original tumor tissue (left) and the corresponding GO (right). (**E**) Necrotic areas in tumor tissue (left) and GO (right) after two weeks in culture. (**F**) Neurons in patient tumor tissue (left) and GO (right), with healthy mitochondria and reticulum network highlighted. (**G**) Oligodendrocytes in tumor tissue (left) and in the derived GO (right), showing glycogen deposits identified in the GO. (**H**) Lipid droplet-rich oligodendrocytes in original tumor tissue (left) and corresponding GO (right), shown in two different patients, with lipid droplets highlighted in blue. (**I**) Neuron-oligodendrocyte interactions observed in GOs after two weeks in culture; neurons (bottom) and oligodendrocytes (top) are indicated by blue arrows. (**J**) Tumor cell identified in a GO after two weeks in culture, with a magnified view of the cytoplasm (right) highlighting mitochondria and the Golgi apparatus

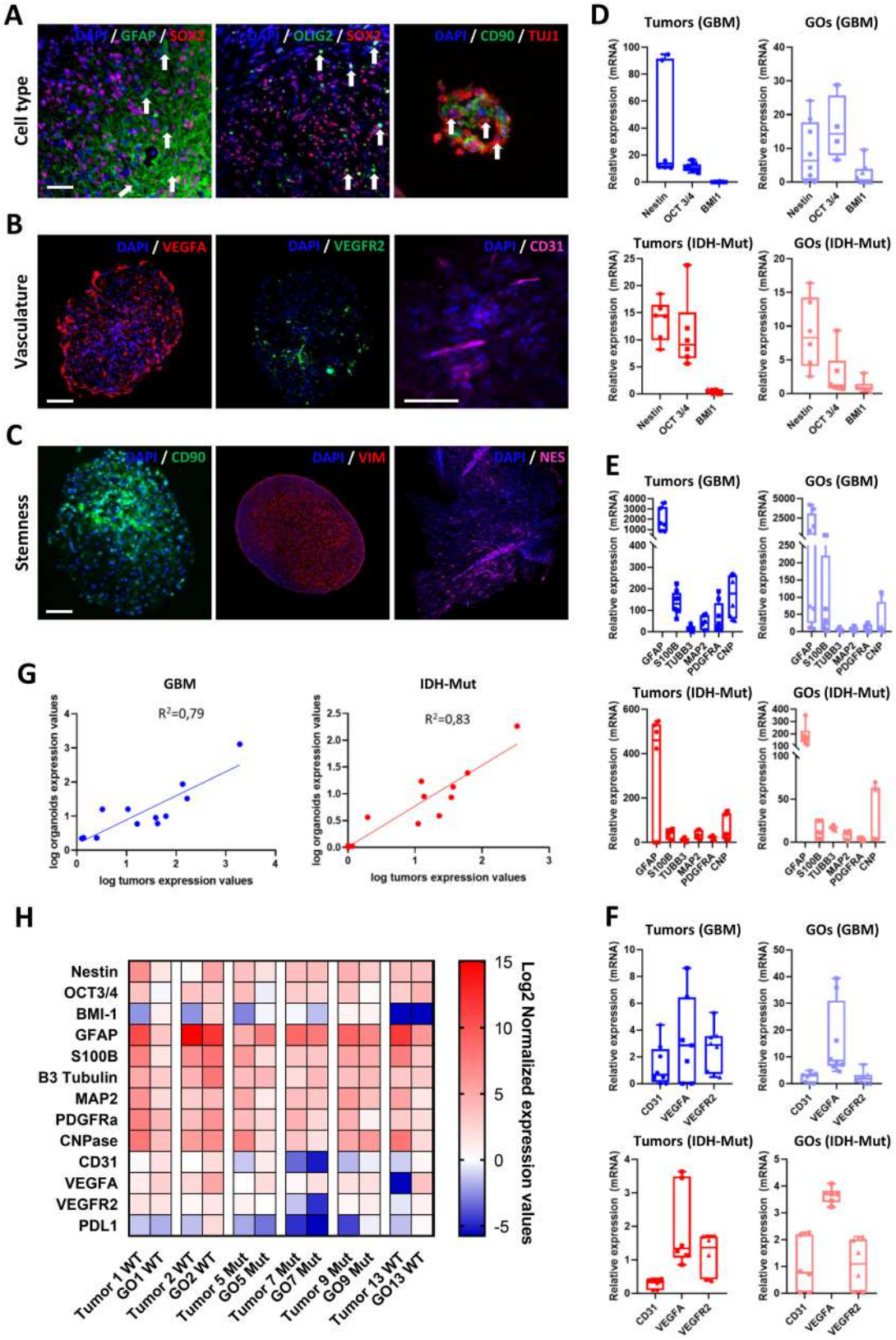

Fig. 4 (See legend on next page.)

(See figure on previous page.)

Fig. 4 Molecular characterization of GOs: (**A**) Immunofluorescence staining of cell type markers in patient-derived GOs: left GFAP (green) and SOX2 (red); center OLIG2 (green) and SOX2 (red); right TUJ1 (red) and CD90 (green), with nuclei counterstained using DAPI (blue); scale bar = 50 µm. White arrows point to astrocytes, oligodendrocytes and neurons, respectively. (**B**) Immunofluorescence staining of microvasculature markers in GOs: VEGFA (red, left), VEGFR2 (green, center), and CD31 (magenta, right), with nuclei counterstained with DAPI (blue); scale bar = 200 µm. (**C**) Immunofluorescence staining of stem cell markers in GOs: CD90 (green, left), VIMENTIN (red, center), and NESTIN (magenta, right), with nuclei counterstained with DAPI (blue); scale bar = 200 µm. (**D–F**) Box plots showing qRT-PCR expression levels of (D) stemness markers (*NESTIN*, *OCT3/4*, *BMI1*), (**E**) cell-type markers (*GFAP*, *S100β*, *TUBB3*, *MAP2*, *PDGFRA*, *CNP*), and (**F**) microvasculature markers (*CD31*, *VEGFA*, *VEGFR2*) in glioma samples. Data is shown for tissue from GBM patients (dark blue) and IDH-mutant patients (dark red), as well as derived GOwts (light blue) and GOmuts (light red). Each point represents an individual organoid, with median, interquartile range (IQR), and standard deviation (SD) indicated. *N* = 6 paired samples in duplicate. (**G**) Linear regression analysis of gene expression between tumor tissue and derived GOs from GBM (left, blue) and IDH-Mut (right, red) samples. Expression values are represented as log-transformed values, with the R^2 value of each regression displayed on the graph. (**H**) Heatmap of log_2-normalized qRT-PCR expression values for the assessed genes, with each pair of columns representing parental tissue (left) and the corresponding GO after two weeks in culture (right). *N* = 6 paired samples.

patterns in each tumor sample were faithfully recapitulated in their paired GOs (Fig. 4H).

GOwts conserve molecular expression and key genetic alterations of parental tissues

To continue our GO molecular characterization, we performed RNA-seq on a representative cohort ($N = 11$) of paired tumors and derived GOwts from GBM tissues, as these represent the majority of cases. First, we assessed differential gene expression (Fig. 5A).

We identified a subset of differentially expressed genes (DEGs) in GOs, primarily associated with metabolic pathways, disease adaptation, environmental response, and molecular transport (Fig. 5B). Moreover, GSEA analysis of these DEGs confirmed upregulation of signatures related to protein secretion, glycolysis and hypoxia in GOs (Fig. S6A). Additionally, we observed that 17088 genes were expressed in both tumors and GOs, constituting 96.2% of the total genes expressed. Conversely, only 287 (1.6%) genes were exclusively expressed in parental tumors and 396 (2.2%) were unique to GOs (Fig. 5C). Gene ontology (GO) analysis of these genes revealed both tumor and GOs exclusive genes related to mostly integral components of cell membranes as well as signaling and response pathways (Fig. 5D and E).

Complementary analyses using Pearson correlation (Fig. S6B) and hierarchical clustering (Fig. S6C) further underscored the strong molecular similarity between GOs and their parental tumors. These data suggest that GOs maintain expression of almost the full gene complement of parental tissues, and uniquely expressed genes may be related to adaptations to their new ex vivo culture environment.

We continued by examining the expression of stromal cell-associated markers and cell activity genes, which closely mirrored our previous results. Moreover, we observed that tumors and paired GOs tend to group together when examining both stromal and activity-related signatures, where we observed consistently high AU values within major tumor-GO clusters (Fig. 5F and G). These findings further reinforce the molecular similarities between GOs and their parental tumors independent of the specific functional gene set analyzed, supporting their relevance as preclinical glioma models.

To evaluate the conservation of the molecular subtype [38] of our model, we analyzed RNA-seq data from paired tumors and GOs using the gene signature refined by Wang et al. [39]. Majority of GOs retained the molecular subtype of their parental tumor, while 4 evolved to the mesenchymal subtype and 1 shifted from proneural to classical (Fig. S6D), in addition, statistical analysis of subtype clustering showed a clear association between tumors and paired GOs (Fig. S6E). This transition may reflect sampling variability due to spatial heterogeneity within tumors or represent dynamic changes occurring in culture that parallel in vivo tumor evolution [40, 41].

We also examined the status of the IDH1 R132H mutation in our GOmut samples, which is currently the only clinically actionable mutation in gliomas and is associated with improved mOS [42, 43]. Unlike established glioma cell lines, which often lose this mutation in culture [44], our GOmuts maintained IDH1 R132H over time. We were able to detect the presence of the mutation in representative GOmuts by IHC, ddPCR, and Sanger sequencing, but not in GOwt controls. Consistent with this, GOmuts exhibited significantly elevated D-2HG levels. Moreover, we verified the long-term stability of this mutation in GO7mut after eight weeks in culture (Fig. S6F-I).

Altogether, these findings establish GOs as reliable models for preserving the molecular identity of gliomas, including key genetic mutations and subtype fidelity.

GOwts recapitulate myeloid-dominant immune profiles and low checkpoint expression found in parental IDH-wt GBM

Given the poor prognosis of gliomas, immunotherapy has been explored as a potential therapeutic option [45]. Several molecular approaches were performed to better understand and characterize the immune landscape of our samples in depth.

Transcriptomic analysis revealed elevated expression of myeloid lineage-associated genes, including microglial and macrophage markers (Fig. 6A), consistent with

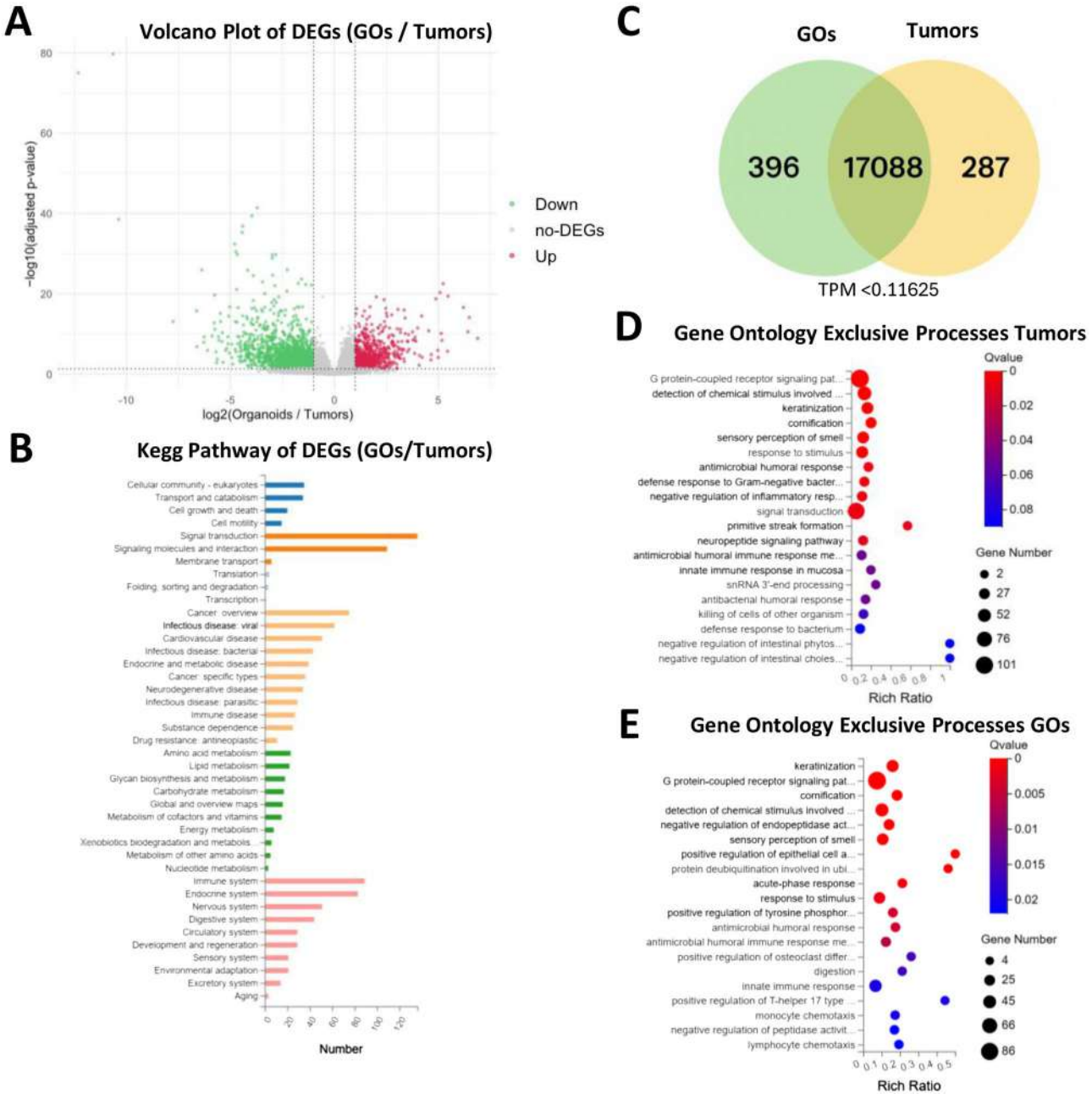

Fig. 5 (continued)

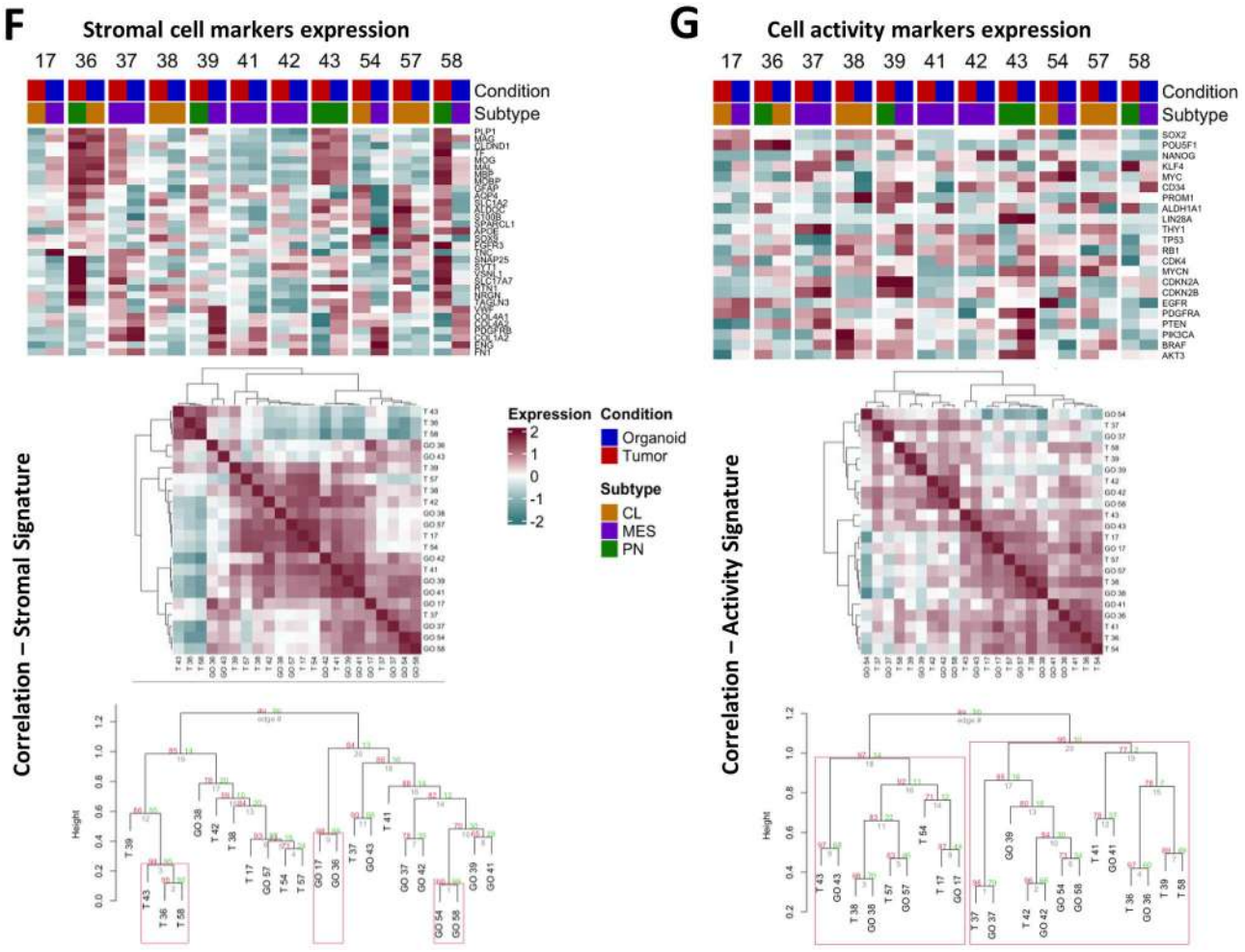

Fig. 5 RNA-seq analysis of GOs from IDH-wt GBM: (**A**) Volcano plot highlighting upregulated (red) and downregulated (green) genes in GOs compared to their parental tumors. Gene expression is represented as $\log_2$ Fold change, with statistical significance shown as -$\log_{10}$ q-value (**B**) Kegg pathway classifications of upregulated genes in GOs, with categories color-coded. (**C**) Venn diagram depicting genes uniquely expressed in GOs (green) and parental tumors (yellow). (**D-E**) Gene Ontology process classification of genes exclusively expressed in tumors (**D**) or GOs (**E**). (**F-G**) Heatmaps displaying z-score normalized expression (top), sample-wise correlations (middle) and hierarchical clustering dendrograms with Approximately Unbiased (AU) p-values computed by pvclust (bottom) of stromal cell markers (**F**) and cell activity markers (**G**) in matched parental tissues (red) and GOs (blue). Samples are color coded according to their molecular subtype: classical (yellow), mesenchymal (purple) and proneural (green). TPM values were scaled by gene-wise z-score normalization (range −2 to 2) to standardize the expression levels across samples. *N* = 11 paired samples

previous observations in gliomas [46, 47]. These findings were validated by IF, where we readily detected IBA1+ microglia and CD68+ macrophages in both tumor tissues and paired GOs (Fig. 6B). Closer inspection of M1/M2 polarization markers [48] by IF identified the presence of M1 and M2 positive microglia in our GOs (Fig. 6C). These two subpopulations were also readily identified in our transcriptomic data in both tumors and derived GOs, with a slight prevalence of M1 markers (Fig. 6A).

In contrast, RNA-seq analyses indicated a lack of lymphoid cells. T-cell markers, including CD3, CD4, and CD8, were expressed at negligible levels across samples (Fig. 6A) and were not detectable by IF (Figs. 6D). Mouse spleen samples were used as positive controls (Fig. S7A). Flow cytometry data confirmed this "cold" immune profile, revealing that only approximately 10% of CD45+ cells were CD3+, with minimal CD4+ or CD8+ subpopulations present (Fig. 6E, S7B and C). This profile was conserved across GOs and their respective tumors.

To further corroborate these observations, we analyzed two publicly available scRNA-seq cohorts (CGGA and Bhaduri), both of which confirmed a minimal presence of lymphoid lineage cells in glioma tissues (Fig. 6G). Additionally, immune cell deconvolution of our bulk RNA-seq data reinforced the prevalence of myeloid populations in both tumors and GOs, while lymphoid cell populations remained sparse, with no significant differences between the two sample types (Fig. 6H).

Interestingly, principal component analysis (PCA) of our RNA-seq data using an immune cell-specific gene

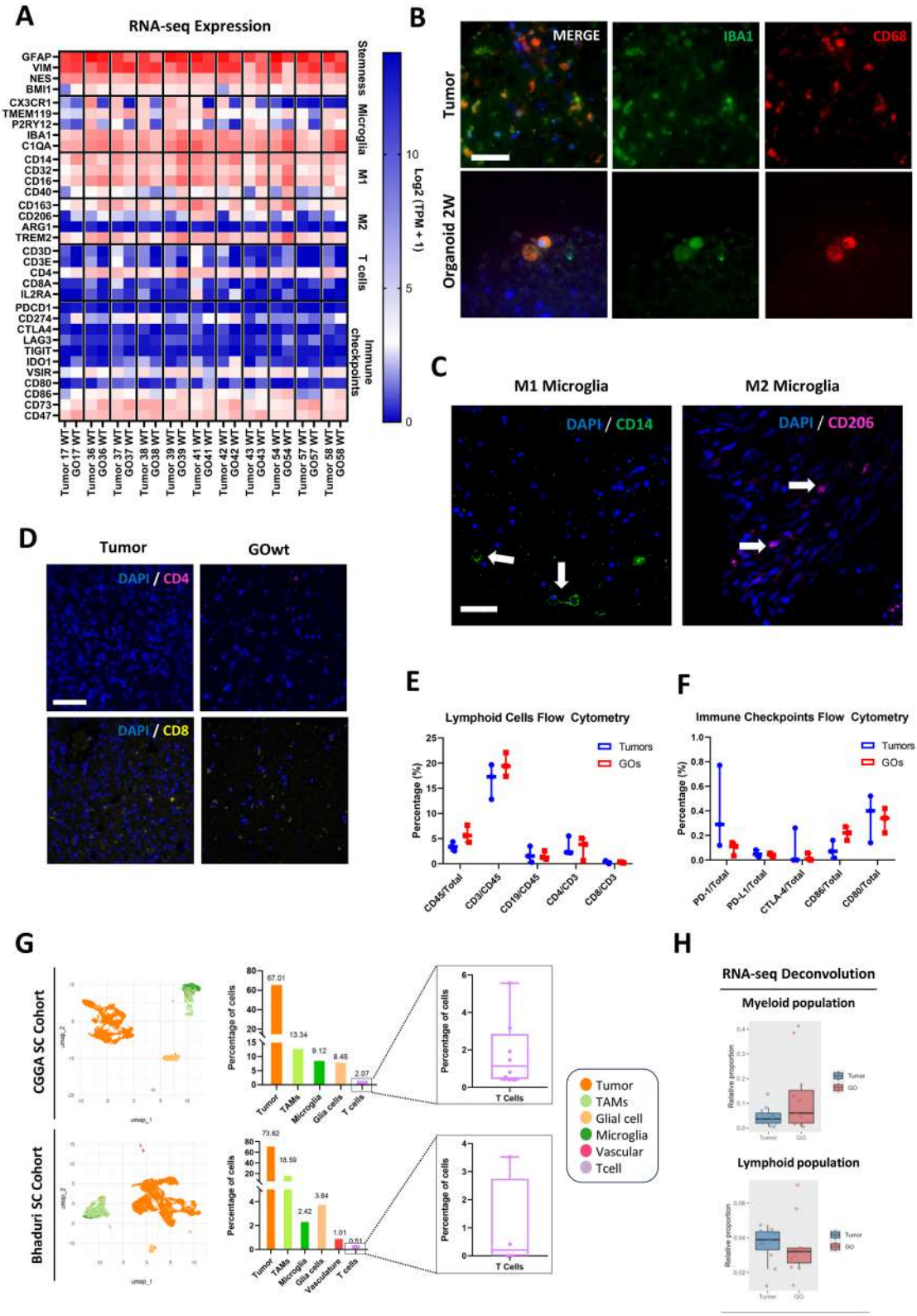

Fig. 6 (See legend on next page.)

(See figure on previous page.)

Fig. 6 GOs derived from IDH-wt GBM replicate "cold" immune phenotype: (**A**) RNA-seq expression levels from 11 parental tumors (left, termed tumors) and their corresponding GOs after 2 weeks in culture (right, termed GO). Color represents log2 of TPM +1 values with a color gradient from blue (lowest expression) to red (highest expression). Selected genes are separated into their function, from top to bottom, stemness, microglia, M1 and M2, T cell and immune checkpoints markers. (**B**) Representative IF for CD68 (red) and IBA1 (green) in parental tumors (top) and derived GOs after 2 weeks in culture (bottom). Counterstained with DAPI (blue). Scale bar is 100 µm. (**C**) Representative IF for M1 marker CD14 (left, green) and M2 marker CD206 (right, magenta) in GOs after 2 weeks in culture. Nuclei are counterstained with DAPI. Scale bar is 50 µm. (**D**) Representative IF for CD4 (top), magenta) and CD8 (bottom, yellow), in both parental tumors (left) and derived GOs after 2 weeks in culture (right). Scale bar is 100 µm. (**E**) Violin plot illustrating immune cell populations identified by flow cytometry in original tissue samples (left, blue) and corresponding derived GOs (right, red). (**F**) Violin plot showing percentage of cells expressing key immune checkpoint markers assessed by flow cytometry in tumor tissue (left, blue) and derived GOs (right, red). (**G**) scRNA-seq analysis of immune cell populations in glioma datasets from the CGGA (top) and Bhaduri (bottom) cohorts. UMAP plot of cell-type distribution (left), bar graph of immune cell proportions (middle), and box plot of T-cell percentages per patient (right). (**H**) Boxplot of RNA-seq deconvolution via CibersortX on myeloid cell population (top) and lymphoid population (bottom) of parental tumors (blue) and GOs (red)

signature revealed that GOs and their parental tumors form two distinct clusters (Fig. S7G). This suggests that while the overall immune landscape is preserved, certain immune components may diverge due to adaptation to ex vivo culture conditions, or due to the deterioration of immune cells after two weeks in culture.

We next investigated the expression of immune checkpoint (IC) proteins, which are often targeted in immunotherapy. RNA-seq and flow cytometry showed minimal expression of classical ICs, including PD-1, PD-L1, CTLA-4, CD80, and CD86, with fewer than 0.8% of total cells expressing these proteins (Figs. 6A, 6F and S7D). These findings were validated by IF, which confirmed the absence of PD-L1 in glioma samples but its presence in a primary B-cell lymphoma used as a positive control (Fig. S7E). qRT-PCR analysis also confirmed low PD-L1 transcript levels in both tumors and GOs (Fig. S7F and 4H). Notably, we did observe clear expression of macrophage-associated ICs CD47 and CD73 (Fig. 6A), which have been described in the GBM context [49].

Collectively, these findings demonstrate that GOs preserve the global immune composition of parental tumors, characterized by dominant myeloid infiltration and lymphocyte deficiency. While transcriptomic analyses reveal culture associated shifts in immune cell states, the conserved myeloid enrichment and low expression of classical immune checkpoints support the fidelity of GOs as a model of glioma immune evasion and help explain the limited efficacy of conventional immune checkpoint therapies in this tumor type.

GOs derived from IDH-wt GBM are resistant to standard chemotherapeutics

We next investigated the response of GOs to antineoplastic agents incorporated into glioma treatment regimens, including TMZ, vincristine, irinotecan, gefitinib, etoposide, and doxorubicin. For this analysis, we focused on GOwts, as GBM is the most prevalent form of glioma with the worst prognosis. To begin, we conducted an *in silico* analysis using our RNA-seq data. This data was analyzed with the bioinformatic tool DiSCoVER [17], which compares expression profiles of tumor samples to predict potential drug sensitivities. The analysis suggested that GOs would be resistant to most of the selected compounds, except for gefitinib, which was predicted to elicit a potential response in all samples with a score of 0.3–0.4, and doxorubicin, with a lower score of 0.15–0.2 (Fig. 7A). These data were further validated in newly established GOs via MTS assay (Fig. 7B) and annexin V/PI apoptosis assay (Fig. 7C). We also observed a notable reduction in the number of cells per mL of gefitinib treated GOs (Fig. S9A)

Histological features of treated GOs remained unchanged when compared to untreated GOs, and we further examined the expression of classical GBM markers (Fig. 7D and E).

No significant vimentin (Fig. 7G) or GFAP (Fig. 7H) level changes were observed among treatments. However, we observed that TMZ and gefitinib treated GOs present a lower nuclei count (Fig. 7F) while TMZ, etoposide, doxorubicin and gefitinib presented significantly higher levels of DNA damage (Fig. 7I).

To assess clinical relevance, we analyzed the clinical progression of patients included in the *in silico* screen. Notably, almost 70% of patients experienced tumor recurrence within 12 months despite receiving SOC treatment (Fig. 7J), aligning with the predicted resistance to TMZ and reinforcing the predictive value of our GO-based model.

DiSCoVER-guided drug screening uncovers alectinib, ruxolitinib and dabrafenib as novel therapeutic candidates for GOs derived from IDH-wt GBM patients

Building on our previous findings, we sought to identify potential therapeutic compounds for GOs. To this end, we selected the 3 compounds with the highest sensitivity score in our computational screening (Fig. 8A). One of them, alectinib, is effective in tumors with high expression of the ALK protein [50], a common phenomenon in gliomas [51, 52]. We confirmed a higher RNA-seq expression of *ALK* in our cohort than in healthy brain tissue (Fig. S8B). Moreover, ALK could also be detected via IHC in GOs (Fig. S8A), confirming target relevance.

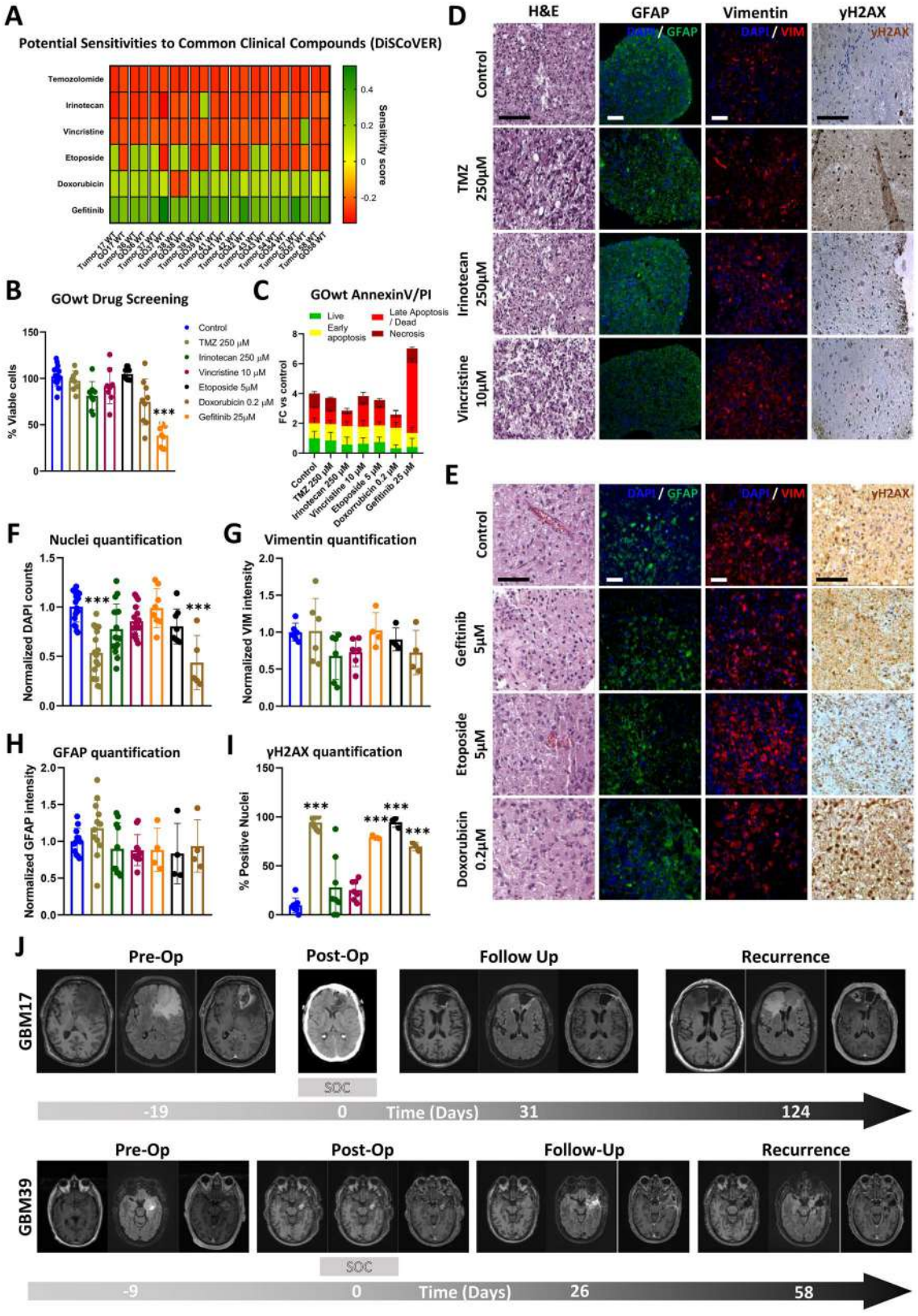

Fig. 7 (See legend on next page.)

(See figure on previous page.)

Fig. 7 GOwts are resistant to standard-of-care chemotherapies: (**A**) Heatmap of predicted drug sensitivities to SOC therapeutic agents. Drugs are listed on the left, and each pair of rows represents a parental tumor and derived GO. Color corresponds to sensitivity score, with dark green representing the potential best responders, and dark red the most resistant samples. (**B**) MTS viability assay after 48 h of treatment. Data is normalized to control. Bars represent mean % of viable cells, with SD. $N = 3$ different GOs per treatment. (**C**) Stacked bar graph of annexin V/PI apoptosis assay on representative GOs after 48 h with the indicated drug concentrations of manually selected compounds. Green represents live cells, yellow for early apoptotic cells, red for late apoptotic/dead cells and brown for necrotic cells. Bar height represents Fold change normalized to control, with error bars indicating SD. (**D** and **E**) Representative H&E, GFAP (green), VIM (red) and γH2AX staining images after 48 hours of treatment. Scale bar is 100 µm. (**F–I**) Quantification of number of nuclei (**F**), VIM (**G**), GFAP (**H**), and γH2AX (**I**) from the images. Data are normalized to respective controls, with bars representing mean values and error bars indicating SD. Statistical significance is indicated as follows: ***$p < 0.001$, **$p < 0.01$, *$p < 0.05$. (**J**) Representative MRI images depicting the clinical progression of patients GBM17 (top) and GBM39 (bottom) following SOC therapy. Sequential scans illustrate tumor evolution across key clinical stages: pre-operative baseline, post-operative status, follow-up period, and recurrence. Timepoints are annotated

We validated the *in silico* predictions in a prospective GO cohort, where we observed a significant reduction of cell viability (Fig. 8B and D) by all 3 compounds, together with a considerable reduction in cells per mL (Fig. S9B). Longer treatment times further decreased cell viability (Fig. S9C). Alectinib exhibited the lowest IC50 value at around 25 µM (Fig. S9D and Supplementary table 5). H&E staining confirmed these observations with a drastic cellularity reduction for alectinib and ruxolitinib (Fig. 8C). These antitumoral effects were reproduced in several other glioma models, such as the patient-derived GSC line GBM38, and 3 immortalized glioma lines (U87, U373, LN229) (Fig. 8E), all cell lines except GBM38, which was the most resistant, had a very similar IC50 compared to GOs at around 20–23 µM, comparable values of ruxolitinib, but GOs and U373 had the highest dabrafenib IC50 values at 112 and 137 µM, respectively (Fig. S9E-G and Supplementary Table 5).

Next, we assessed the impact of these compounds on cellular migration of our GOs using a transwell assay (Fig. 8F), which showed that all compounds produced a significant reduction in migration capabilities (Fig. 8G). These strong antimigratory effects of all compounds were corroborated via wound healing assays, except for dabrafenib in U373 (Fig. 8H and I).

Alectinib concentration was reduced from 50 µM to 10 and 25 µM for this experiment, as 24 h with this higher concentration was lethal (Fig. S10A).

To better understand how these compounds affected our GOs, we performed RNA-seq following treatment. GSEA analysis showed that all treatments were affecting key oncogenic pathways. Alectinib downregulated genes targeted by the transcription factor *MYC*, as well as key pathways for cell division, like the G2/M checkpoint and genes involved in the formation of the mitotic spindle, while simultaneously upregulating apoptosis via caspases, the TNFα and hypoxia response pathways. Ruxolitinib produced a significant downregulation of the PI3K signaling pathway, as well as TGFβ1 signaling and DNA repair mechanisms. On the other hand, we identified a single significantly upregulated pathway in the form of angiogenesis. Finally, dabrafenib affected key replication and growth pathways, while also altering the metabolism of the tumor (Fig. 8J and S10B).

Moreover, we included an in vivo validation with heterotopic models of both GOs and U87 cells. Our data showed that alectinib and ruxolitinib led to a significant reduction in tumor progression (Fig. 8K) as well as endpoint size (Fig. 8L and M). These results highlight the effectiveness of these 2 compounds in an in vivo model.

In short, we identified three compounds which showed great antitumoral effects in vitro in both GOs and cell lines, reducing viability, affecting migration capacity and altering key tumoral pathways, while alectinib and ruxolitinib also reduced tumor growth in vivo.

Discussion

The development of reliable preclinical models that faithfully replicate the cellular and molecular complexity of gliomas remains a critical unmet need in neuro-oncology. Current methods show low maintenance of tumor stromal cells and spatial heterogeneity and have low success rates for IDH-Mutgliomas, making them inadequate platforms for studying clinically relevant tumor biology [53].

In this study, we demonstrate that GOs preserve key histological features, cellular heterogeneity, and microenvironmental interactions of their parental tumors, including clinically relevant mutations and immune profiles. By integrating this model with transcriptomic-guided drug prediction using the DiSCoVER platform, we uncover novel therapeutic candidates with confirmed antitumor efficacy in vitro and in vivo. This approach contributes to glioma modeling and could support the future design of personalized clinical trials aimed at improving outcomes in these highly resistant and heterogeneous tumors.

Our overall success rate in GO establishment aligns with previous reports [20, 42]. We were able to successfully generate GOs from IDH-Mut gliomas, something challenging given their lower proliferation rate and less aggressive nature compared to GBM [1], with a much higher establishment rate than traditional glioma cell lines [54]. This efficiency positions GOs as a superior platform for modeling both GBM and IDH-Mut gliomas in vitro. Notably, our results suggest that a defined establishment time, seeding density, and GO size should be

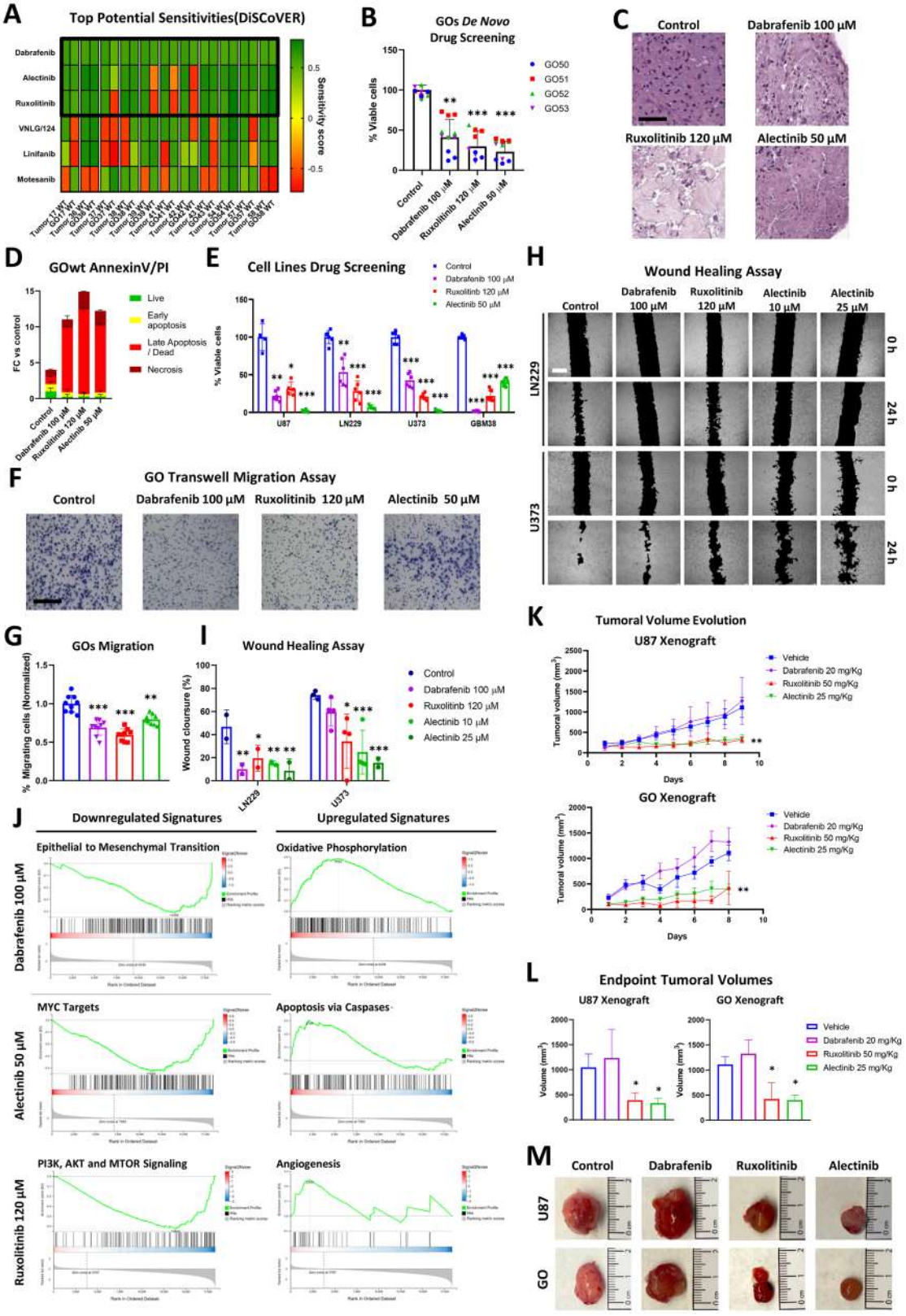

Fig. 8 (See legend on next page.)

(See figure on previous page.)

Fig. 8 *De novo* screening identifies Alectinib, Ruxolitinib and Dabrafenib as potential glioma therapies: (**A**) Heatmap showing predicted drug sensitivities for the top six most promising compounds identified by DiSCoVER. Compounds are listed on the left, with each pair of rows representing a matched tumor tissue and its derived GO. Sensitivity scores are color-coded, with dark green indicating higher predicted sensitivity and dark red representing lower predicted sensitivity. $N = 11$ paired samples. (**B**) MTS viability assay assessing the effects of alectinib, ruxolitinib, and dabrafenib on a prospective cohort of freshly derived GOs ($N = 4$) after 48 hours of treatment. Each GO was tested in triplicate, and all values were normalized to their respective untreated control. Mean viability values and SD are represented, as well as triplicates from patients, which are color coded. (**C**) Representative H&E images of GOs treated with dabrafenib, ruxolitinib and alectinib. Scale bar is 100 µm. (**D**) Stacked bar graph of annexin V/PI apoptosis assay on representative GOs after 48 h with the indicated drug concentrations of compounds selected via DiSCoVER. Green represents live cells, yellow for early apoptotic cells, red for late apoptotic/dead cells and brown for necrotic cells. Bar height represents Fold change normalized to control, with error bars indicating SD. (**E**) MTS viability assay of alectinib, ruxolitinib and dabrafenib in established glioma cell lines (U87, LN229 and U373) and GSCs (GBM38). All values are normalized to their respective control. Each replicate is shown individually. (**F**) Representative brightfield images of GO transwell migration assay. GOs were dissociated into single-cell suspensions, seeded into transwell inserts, and treated with the corresponding drug for 6 hours. Scale bar is 200 µm. (**G**) Quantification of migrated cells following treatment ($N = 3$ independent patients GOs). Migration values are normalized to their respective untreated control. (**H**) Representative brightfield images from the wound healing assay at baseline and 24 hours post-treatment in LN229 (top) and U373 (bottom) cells scale bar represents 500 µm. (**I**) Quantification of wound closure in LN229 and U373 cells after 24 hours of treatment with ruxolitinib (red), alectinib (green), and dabrafenib (purple) (J) GSEA plots of hallmark signatures significantly downregulated (left) or upregulated (right) following GO treatment with alectinib (top), ruxolitinib (middle), and dabrafenib (bottom). Green lines show enrichment profiles; black bars indicate gene signature hits; grey curves represent gene ranking scores; blue to red scale shows signal-to-noise ratio of hits. (**K**) Tumor growth curves for in vivo xenografts. Each point represents the relative mean tumoral volume each day with SEM. Mice were treated daily with vehicle (blue), ruxolitinib 50 mg/kg (red), alectinib 25 mg/kg (green) and dabrafenib 20 mg/kg (purple). $N = 3$ mice per group. Samples were subjected to two-way ANOVA with daily mean comparison to determine statistical significance. (**L**) Bar graph of tumor volumes at experimental endpoint. Volumes (mm^3) are shown for vehicle (blue), ruxolitinib 50 mg/kg (red), alectinib 25 mg/kg (green), and dabrafenib 20 mg/kg (purple). Bars represent mean ± SEM. (**M**) Representative images of extracted tumors at endpoint, ruler is in cm. Statistical significance is indicated as follows: $^{***}p < 0.001$, $^{**}p < 0.01$, $^{*}p < 0.05$

determined to ensure their suitability as a drug screening platform.

Although Jacob et al. [18, 19] highlighted the potential for biobanking patient-derived GOs, our results demonstrate that, while biobanked GOs preserve the histological characteristics of their parental tumors and freshly established GOs, their proliferation is significantly diminished when recovered in vitro. This observation aligns with reports from other studies utilizing this model [55, 56], where growth rates post-biobanking recovery are not explicitly described. This limitation may have implications for the utility of biobanked GOs in longitudinal studies. However, we observed that subcutaneous implantation of biobank recovered undissociated GOs in athymic mice is a viable way of expanding the model in vivo for downstream applications like drug testing.

To our knowledge, this is the first study to perform TEM on this model of GOs, revealing ultrastructural features of cellular microarchitecture within GOs. TEM analysis revealed a diverse array of cell populations within the GOs, including neurons and other glial cells, as well as intact organelles and preserved cell-cell interactions, mirroring physiological conditions [57], emphasizing the complexity of this model compared to traditional cell lines, which lack such interactions [58].

Given the potential of immunotherapy to revolutionize malignant glioma treatment, we examined the immune landscape of our models and their parental tumors. Both our patient tumors and their matched GOs showed an immune system dominated by myeloid cells, with both M1 and M2 microglia subpopulations present, and almost no lymphoid ($CD4^+/CD8^+$) infiltration, exactly as reported for GBM in vivo [59, 60]. Classical immune-checkpoint molecules (PD-1, PD-L1, CTLA-4, CD80, CD86) were barely detectable in either sample type, matching the poor clinical performance of checkpoint blockade in glioma [61, 62], as well as other studies where these markers are analyzed in gliomas [63, 64].

However, there are two limitations to our immune profile. First, we did not pre-enrich $CD45^+$ cells like other studies [65, 66], so the scarce T-cell populations may be under-represented. Second, GOs were generated from densely cellular tumor cores; infiltrative margins (where lymphoid cells are relatively richer and more active) [67, 68] were not sampled.

Next, we assessed GOs responses to SOC therapies. As anticipated and coinciding with our *in silico* results, the standard chemotherapy treatments did not produce significant reductions in cellular viability, mirroring previously described clinical outcomes [69, 70], as well as the evolution of patients included in the screening, and previous studies using the same model or simpler GSC models [33, 71]. This resistance underscores the urgent need for alternative therapeutic strategies. Additionally, when screening for lesser used compounds like gefitinib we observed a marked reduction in cellular viability, which also coincided with our *in silico* results. An explanation for this evasion of DNA damage could be that tumoral cells in GOs undergo a transformation into senescent cells after being challenged by DNA damaging agents like TMZ, as some authors have pointed out [72, 73].

To explore alternative therapeutic options, we performed *de novo* drug screening using the DiSCoVER platform, integrating RNA-seq data from paired tumor and organoid samples. This analysis identified three promising candidates: the ALK1 inhibitor alectinib, the JAK

inhibitor ruxolitinib, and the BRAF inhibitor dabrafenib. Among these, alectinib exhibited the strongest cytotoxic effect, followed closely by ruxolitinib, which was the most effective at inhibiting migration, with dabrafenib ranking second in this regard. These compounds also affected critical pathways for cancer development in vitro. When assessed in vivo, alectinib and ruxolitinib significantly affected tumoral growth of both GOs and U87 cells. These are proof-of-concept therapeutic prioritizations, not yet validated as patient outcome predictors.

Interestingly, a recent clinical trial has demonstrated ruxolitinib safety in a small cohort of 60 patients (NCT03514069) highlighting its potential to be integrated into clinical practice [74]. Similarly, alectinib has shown encouraging results in other tumors, such as neuroblastoma [75], and is currently being investigated in a phase I/II trial for treatment-resistant CNS tumors in children and adolescents [76], with the added benefit of being fully permeable to the blood brain barrier. Finally, dabrafenib has been reported as an effective therapeutic agent restricted to patients with altered *BRAF*, limiting its applicability as a broader treatment option [77, 78].

Conclusions

In conclusion, GOs present limitations in proliferative capacities and biobanking efficiency that must be addressed to enable clinical implementation. Nonetheless, GOs represent an invaluable preclinical tool. Our findings further support GOs as a robust model that recapitulates the cellular, molecular, and histological complexity of gliomas. By integrating this model with bioinformatic drug prediction, we demonstrated its utility in personalized drug screening and uncovered novel therapeutic opportunities, in a short timeframe relevant to clinical practice. These findings support the potential of GOs to inform clinical decision-making and accelerate the development of more effective, individualized therapies for glioma patients. Based on our findings, we propose alectinib and ruxolitinib as candidate therapeutics warranting further clinical investigation in gliomas.

Abbreviations

IDH	Isocitrate dehydrogenase
GBM	IDH-wild type glioblastoma
mOS	Median overall survival
SOC	Standard of care therapy
TMZ	Temozolomide
PDX	Patient-derived xenograft
GO	Malignant glioma organoid
GOmut	IDH-mutant organoids
GOwt	GBM organoids
GSCs	Glioma stem-like cells
PFA	Paraformaldehyde
H&E	Hematoxylin and eosin
IF	Immunofluorescence
IHC	Immunohistochemistry
BrdU	Bromodeoxyuridine
qRT-PCR	Quantitative real time PCR
ddPCR	Droplet digital PCR
FC	Flow cytometry
TEM	Transmission electron microscopy
RNA-seq	RNA sequencing
scRNA-seq	Single cell RNA sequencing
ECM	Extracellular matrix
PI	Propidium iodide
D-2HG	D-2-Hydroxyglutarate
PAS	Periodic acid-Schiff

Supplementary information

The online version contains supplementary material available at https://doi.org/10.1186/s40364-026-00894-3.

Supplementary Material 1

Supplementary Material 2

Supplementary Material 1

Supplementary Material 4

Supplementary Material 5

Supplementary Material 6

Supplementary Material 7

Acknowledgements

We would like to acknowledge the expertise and assistance of the Histology Unit at San Pablo CEU (Madrid, Spain) in all histological preparations. We also thank the Electron Microscopy Unit at Centro de Biología Molecular Severo Ochoa (Madrid, Spain) for their support in interpreting electron microscopy images. The authors wish to thank the donors, and the Hospital Universitario Puerta de Hierro Majadahonda (HUPHM)/Instituto de Investigación Sanitaria Puerta de Hierro-Segovia de Arana (IDIPHISA) Biobank (Carlos III Health Institute Biomodels and Biobanks Platform – PT23/00015) for the human specimens used in this study.

Author contributions

AAS and NGR conceived the research concepts and designed the original experiments. AMS, LMM, JCN, CMR, MCP and PSG conducted experiments, while AMS and NGR performed data analysis. AHM performed RNA-seq and scRNA-seq analysis. Clinical samples, patient diagnoses and MRI images were provided by RGG, NL, RPA, SGRM, CAG, APN and AJSL. FPR confirmed diagnoses and contributed to the blind analysis of histological preparations. BMJ performed electron microscopy sample preparation and image acquisition. MVPF performed RNA-seq deconvolution. AMS and NGR wrote the manuscript, and all authors participated in manuscript review and editing.

Funding

This study has been funded by Instituto de Salud Carlos III (ISCIII) and co-funded by the European Union through the projects "PI21/01353" and PT23/00015 (ISCIII Platform for Biomodels and Biobanks-Organoids Hub) to NGR and AAS, and PI21CIII/00002 to PSG. AMS was supported by the Ministry for Universities, Spain (FPU21/02281). AHM is supported by a predoctoral fellowship from Universidad Francisco de Vitoria. MCP was supported by the Young Employment Initiative (Comunidad de Madrid). The publication is part of the CPP2023-010432 project funded by MICIU/AEI/10.13039/501100011033 and the EU's FEDER.

Data availability

RNA-seq datasets are publicly available at Gene Expression Omnibus (GEO) under accession code GSE303683.

Declarations

Ethics approval

Ethical approval for the use of these samples was granted by the institutional review board of HM Hospitals (CEIm No: 23.06.2206-GHM) and Hospital 12 de Octubre (CEI 21/480). All patients provided informed written consent

prior to enrollment, and all procedures were conducted in accordance with the principles of the Declaration of Helsinki. All animal experiments were performed under PROEX 142.8/24 in compliance with Directive 2010/63/EU of the European Parliament and of the Council on the protection of animals used for scientific purposes, as well as other applicable national and institutional regulations, ensuring the highest standards of animal welfare and ethical research practices.

Consent for publication
Not applicable.

Competing interests
The authors declare no competing interests.

Author details
[1]Faculty of Experimental Sciences, Universidad Francisco de Vitoria, Madrid, Spain
[2]Brain Tumor Laboratory, Fundación Vithas, Grupo Hospitales Vithas, Madrid, Spain
[3]Neuro-Oncology Unit, Instituto de Salud Carlos III-UFIEC, Madrid, Spain
[4]PhD Programme on Biomedical Sciences and Public Health, Universidad Nacional de Educación a Distancia, UNED-ISCIII, Madrid 28040, Spain
[5]Department of Neurosurgery, Hospital Universitario Puerta de Hierro, IDIPHISA, Madrid, Spain
[6]Department of Surgery, Faculty of Medicine, Autonomous University of Madrid, Madrid, Spain
[7]Department of Neurosurgery, Hospital La Fe, Valencia, Spain
[8]Hospital Universitario Quironsalud, Madrid, Spain
[9]Department of Neurosurgery, Hospital Universitario 12 de Octubre, Madrid, Spain
[10]Department of Surgery, Universidad Complutense de Madrid, Facultad de Medicina, Madrid, Spain
[11]Fundación de Investigación HM Hospitales, Anatomía Patológica HM Hospitales, Madrid, Spain
[12]Faculty of Health Sciences, HM Hospitals, CUHMED, Universidad Camilo Jose Cela, Madrid, Spain
[13]Electron Microscopy Unit, Centro Nacional de Biotecnología (CNB-CSIC), Campus de Cantoblanco, Universidad Autónoma de Madrid, Madrid 28049, Spain
[14]Neuroimmunology Unit, Instituto de Investigación Sanitaria Puerta de Hierro-Segovia de Arana, Madrid 28222, Spain
[15]Biobank, Instituto de Investigación Sanitaria Puerta de Hierro-Segovia de Arana, Madrid 28222, Spain
[16]Faculty of Medicine, Universidad Francisco de Vitoria, Madrid, Spain
[17]Preclinical Models of Brain Tumors Lab (BTL), Unidad Funcional de Enfermedades Crónicas (UFIEC), Instituto de Salud Carlos III (ISCIII), Madrid, Spain

Received: 26 August 2025 / Accepted: 11 January 2026
Published online: 06 February 2026

References

1. Louis DN, Perry A, Wesseling P, et al. The 2021 WHO classification of tumors of the central nervous system: a summary. Neuro Oncol. 2021;23(8):1231–51.
2. Li R, Chen X, You Y, et al. Comprehensive portrait of recurrent glioblastoma multiforme in molecular and clinical characteristics. Oncotarget. 2015;6(31):30968–74.
3. Ostrom QT, Cioffi G, Waite K, Kruchko C, Barnholtz-Sloan JS. CBTRUS statistical report: primary brain and other central nervous system tumors diagnosed in the United States in 2014-2018. Neuro Oncol. 2021;23(12 Suppl 2):iii1–iii105.
4. Tan AC, Ashley DM, López GY, Malinzak M, Friedman HS, Khasraw M. Management of glioblastoma: state of the art and future directions. CA Cancer J Clin. 2020;70(4):299–312.
5. Stupp R, Mason WP, van den Bent MJ, et al. Radiotherapy plus concomitant and adjuvant temozolomide for glioblastoma. N Engl J Med. 2005;352(10):987–96.
6. Yvone GM, Breunig JJ. Pediatric low-grade glioma models: advances and ongoing challenges. Front Oncol. 2024;13:1346949.
7. de Blank P, Fouladi M, Huse JT. Molecular markers and targeted therapy in pediatric low-grade glioma. J Neurooncol. 2020;150(1):5–15.
8. Pant A, Lim M. CAR-T therapy in GBM: current challenges and avenues for improvement. Cancers. 2023;15(4):1249.
9. Sanders S, Debinski W. Challenges to successful implementation of the immune checkpoint inhibitors for treatment of glioblastoma. Int J Mol Sci. 2020;21(8):2759.
10. Slika H, Karimov Z, Alimonti P, Abou-Mrad T, De Fazio E, Alomari S, et al. Preclinical models and technologies in glioblastoma research: evolution, current state, and future avenues. Int J Mol Sci. 2023;24(22):16316.
11. Veninga V, Voest EE. Tumor organoids: opportunities and challenges to guide precision medicine. Cancer Cell. 2021;39(9):1190–201.
12. Driehuis E, Kretzschmar K, Clevers H. Establishment of patient-derived cancer organoids for drug-screening applications. Nat Protoc. 2020;15(10):3380–409.
13. Pasupuleti V, Vora L, Prasad R, Nandakumar DN, Khatri DK. Glioblastoma preclinical models: strengths and weaknesses. Biochim Biophys Acta Rev Cancer. 2024;1879(1):189059.
14. Seashore-Ludlow B, Rees MG, Cheah JH, et al. Harnessing connectivity in a large-scale small-molecule sensitivity dataset. Cancer Discov. 2015;5(11):1210–23.
15. Barretina J, Caponigro G, Stransky N, et al. The cancer cell line encyclopedia enables predictive modelling of anticancer drug sensitivity. Nature. 2012;483(7391):603–07.
16. Yang W, Soares J, Greninger P, et al. Genomics of Drug Sensitivity in Cancer (GDSC): a resource for therapeutic biomarker discovery in cancer cells. Nucleic Acids Res. 2013;41(Database issue):D955–61.
17. Hanaford AR, Archer TC, Price A, et al. DiSCoVERing innovative therapies for rare tumors: combining genetically accurate disease models with in silico analysis to identify novel therapeutic targets. Clin Cancer Res. 2016;22(15):3903–14.
18. Jacob F, Salinas RD, Zhang DY, et al. A patient-derived glioblastoma organoid model and biobank recapitulates inter- and intra-tumoral heterogeneity. Cell. 2020;180(1):188–204.e22.
19. Jacob F, Ming GL, Song H. Generation and biobanking of patient-derived glioblastoma organoids and their application in CAR T cell testing. Nat Protoc. 2020;15(12):4000–33.
20. Suzuki R, Shimodaira H. Pvclust: an R package for assessing the uncertainty in hierarchical clustering. Bioinformatics. 2006;22(12):1540–42.
21. Bowman RL, Wang Q, Carro A, Verhaak RGW, Squatrito M. GlioVis data portal for visualization and analysis of brain tumor expression datasets. Neuro Oncol. 2017;19(1):139–41.
22. Yu K, Hu Y, Wu F, et al. Surveying brain tumor heterogeneity by single-cell RNA-sequencing of multi-sector biopsies. Natl Sci Rev. 2020;7(8):1306–18.
23. Ruiz-Moreno C, Salas SM, Samuelsson E, et al. Charting the single-cell and spatial landscape of IDH-wild-type glioblastoma with GBmap. Neuro Oncol. 2025;27(9):2281–95.
24. Hao Y, Stuart T, Kowalski MH, et al. Dictionary learning for integrative, multimodal and scalable single-cell analysis. Nat Biotechnol. 2024;42(2):293–304.
25. McGinnis CS, Murrow LM, Gartner ZJ. DoubletFinder: doublet detection in single-cell RNA sequencing data using artificial nearest neighbors. Cell Syst. 2019;8(4):329–37.
26. Yang S, Corbett SE, Koga Y, et al. Decontamination of ambient RNA in single-cell RNA-seq with decontX. Genome Biol. 2020;21(1):57.
27. Korsunsky I, Millard N, Fan J, et al. Fast, sensitive and accurate integration of single-cell data with Harmony. Nat Methods. 2019;16(12):1289–96.
28. De Falco A, Caruso F, Su XD, Iavarone A, Ceccarelli M. A variational algorithm to detect the clonal copy number substructure of tumors from scRNA-seq data. Nat Commun. 2023;14(1):1074.
29. Aran D, Looney AP, Liu L, et al. Reference-based analysis of lung single-cell sequencing reveals a transitional profibrotic macrophage. Nat Immunol. 2019;20(2):163–72.
30. Newman AM, Steen CB, Liu CL, et al. Determining cell type abundance and expression from bulk tissues with digital cytometry. Nat Biotechnol. 2019;37(7):773–82.
31. Couturier CP, Ayyadhury S, Le PU, et al. Single-cell RNA-seq reveals that glioblastoma recapitulates a normal neurodevelopmental hierarchy. Nat Commun. 2020;11(1):3406.
32. Digre A, Lindskog C. The Human Protein Atlas-Spatial localization of the human proteome in health and disease. Protein Sci. 2021;30(1):218–33.
33. García-Romero N, González-Tejedo C, Carrión-Navarro J, et al. Cancer stem cells from human glioblastoma resemble but do not mimic original tumors after in vitro passaging in serum-free media. Oncotarget. 2016;7(40):65888–901.

34. Suarez-Arnedo A, Torres Figueroa F, Clavijo C, Arbeláez P, Cruz JC, et al. An image J plugin for the high throughput image analysis of in vitro scratch wound healing assays. PLoS ONE. 2020;15(7):e0232565.
35. Gordon J, Amini S, White MK. General overview of neuronal cell culture. Methods Mol Biol. 2013;1078:1–8.
36. Roehlecke C, Schmidt MHH. Tunneling nanotubes and tumor microtubes in cancer. Cancers. 2020;12(4):857.
37. Wang X, Liang J, Sun H. The network of tumor microtubes: an improperly reactivated neural cell network with stemness feature for resistance and recurrence in gliomas. Front Oncol. 2022;12:921975.
38. Komori T. The 2016 WHO classification of tumours of the Central Nervous System: the major points of revision. Neurol Med Chir (Tokyo). 2017;57(7):301–11.
39. Wang Q, Hu B, Hu X, et al. Tumor evolution of glioma-intrinsic gene expression subtypes associates with immunological changes in the microenvironment. Cancer Cell. 2017;32(1):42–56.
40. Bhat KPL, Balasubramaniyan V, Vaillant B, et al. Mesenchymal differentiation mediated by NF-κB promotes radiation resistance in glioblastoma. Cancer Cell. 2013;24(3):331–46.
41. Kim Y, Varn FS, Park SH, et al. Perspective of mesenchymal transformation in glioblastoma. Acta Neuropathol Commun. 2021;9(1):50.
42. Reardon DA, Weller M. Vaccination for IDH-mutant tumors: a novel therapeutic approach applied to glioma. Med (N Y). 2021;2(5):450–52.
43. Platten M, Bunse L, Wick A, et al. A vaccine targeting mutant IDH1 in newly diagnosed glioma. Nature. 2021;592(7854):463–68.
44. Piaskowski S, Bienkowski M, Stoczynska-Fidelus E, et al. Glioma cells showing IDH1 mutation cannot be propagated in standard cell culture conditions. Br J Cancer. 2011;104(6):968–70.
45. Liu Y, Zhou F, Ali H, et al. Immunotherapy for glioblastoma: current state, challenges, and future perspectives. Cell Mol Immunol. 2024;21:1354–75.
46. Bonaventura P, Shekarian T, Alcazer V, et al. Cold tumors: a therapeutic challenge for immunotherapy. Front Immunol. 2019;10:168.
47. Hambardzumyan D, Gutmann DH, Kettenmann H. The role of microglia and macrophages in glioma maintenance and progression. Nat Neurosci. 2016;19(1):20–27.
48. Jurga AM, Paleczna M, Kuter KZ. Overview of general and discriminating markers of differential microglia phenotypes. Front Cell Neurosci. 2020;14:198.
49. Brom VC, Burger C, Wirtz DC, Schildberg FA. The role of immune checkpoint molecules on macrophages in cancer, infection, and autoimmune pathologies. Front Immunol. 2022;13:837645.
50. Alam MW, Borenäs M, Lind DE, et al. Alectinib, an anaplastic lymphoma kinase inhibitor, abolishes ALK activity and growth in ALK-positive neuroblastoma cells. Front Oncol. 2019;9:579.
51. Chiba R, Akiya M, Hashimura M, et al. ALK signaling cascade confers multiple advantages to glioblastoma cells through neovascularization and cell proliferation. PLoS One. 2017;12(8):e0183516.
52. Azab MA. Expression of Anaplastic Lymphoma Kinase (ALK) in glioma and possible clinical correlations. A retrospective institutional study. Cancer Treat Res Commun. 2023;36:100703.
53. Peng T, Ma X, Hua W, et al. Individualized patient tumor organoids faithfully preserve human brain tumor ecosystems and predict patient response to therapy. Cell STEM Cell. 2025;32(4):652–69.
54. Mullins CS, Schneider B, Stockhammer F, Krohn M, Classen CF, Linnebacher M. Establishment and characterization of primary glioblastoma cell lines from fresh and frozen material: a detailed comparison. PLoS ONE. 2013;8(8):e71070.
55. Abdullah KG, Bird CE, Buehler JD, et al. Establishment of patient-derived organoid models of lower-grade glioma. Neuro Oncol. 2022;24(4):612–23.
56. Zhou L, Yang J, Wang S, et al. Generation and banking of patient-derived glioblastoma organoid and its application in cancer neuroscience. Am J Cancer Res. 2024;14(10):5000–10.
57. Oliveira B, Çerağ Yahya A, Novarino G. Modeling cell-cell interactions in the brain using cerebral organoids. Brain Res. 2019;1724:146458.
58. Kim J, Koo BK, Knoblich JA. Human organoids: model systems for human biology and medicine. Nat Rev Mol Cell Biol. 2020;21(10):571–84.
59. Kmiecik J, Poli A, Brons NH, et al. Elevated CD3+ and CD8+ tumor-infiltrating immune cells correlate with prolonged survival in glioblastoma patients despite integrated immunosuppressive mechanisms in the tumor microenvironment and at the systemic level. J Neuroimmunol. 2013;264(1–2):71–83.
60. Woroniecka K, Chongsathidkiet P, Rhodin K, et al. T-Cell exhaustion signatures vary with tumor type and are severe in glioblastoma. Clin Cancer Res. 2018;24(17):4175–86.
61. Filley AC, Henriquez M, Dey M. Recurrent glioma clinical trial, CheckMate-143: the game is not over yet. Oncotarget. 2017;8(53):91779–94.
62. Omuro A, Brandes AA, Carpentier AF, et al. Radiotherapy combined with nivolumab or temozolomide for newly diagnosed glioblastoma with unmethylated MGMT promoter: an international randomized phase III trial. Neuro Oncol. 2023;25(1):123–34.
63. Parney IF, Waldron JS, Parsa AT. Flow cytometry and in vitro analysis of human glioma-associated macrophages. Laboratory investigation. J Neurosurg. 2009;110(3):572–82.
64. González-Tablas Pimenta M, Otero Á, Arandia Guzman DA, et al. Tumor cell and immune cell profiles in primary human glioblastoma: impact on patient outcome. Brain Pathol. 2021;31(2):365–80.
65. Hu L, Chen X, Chen M, et al. Enrichment and detection of circulating tumor cells by immunomagnetic beads and flow cytometry. Biotechnol Lett. 2021;43(1):25–34.
66. Perret R, Sierro SR, Botelho NK, et al. Analysis of tumor-infiltrating lymphocytes following CD45 enrichment. Bio Protoc. 2014;4(16):e 1218.
67. Loussouarn D, Oliver L, Salaud C, et al. Spatial distribution of immune cells in primary and recurrent glioblastoma: a small case study. Cancers (Basel). 2023;15(12):3256.
68. Schmassmann P, Roux J, Dettling S, et al. Single-cell characterization of human GBM reveals regional differences in tumor-infiltrating leukocyte activation. eLife. 2023;12:RP92678.
69. Lee SY. Temozolomide resistance in glioblastoma multiforme. Genes Dis. 2016;3(3):198–210.
70. Singh N, Miner A, Hennis L, Mittal S. Mechanisms of temozolomide resistance in glioblastoma - a comprehensive review. Cancer Drug Resist. 2021;4(1):17–43.
71. Majc B, Habič A, Malavolta M, et al. Patient-derived tumor organoids mimic treatment-induced DNA damage response in glioblastoma. iScience. 2024;27(9):110604.
72. Knizhnik AV, Roos WP, Nikolova T, et al. Survival and death strategies in glioma cells: autophagy, senescence and apoptosis triggered by a single type of temozolomide-induced DNA damage. PLoS ONE. 2013;8(1):e55665.
73. Pawlowska E, Szczepanska J, Szatkowska M, Blasiak J. An interplay between senescence, apoptosis and autophagy in glioblastoma multiforme-role in pathogenesis and therapeutic perspective. Int J Mol Sci. 2018;19(3):889.
74. Ahluwalia MS, Ozair A, Khosla AA, Rauf Y, Wei W, Murphy ES, et al. Safety and feasibility of JAK inhibitor ruxolitinib in newly-diagnosed high-grade gliomas (CRUX): final toxicity report. J Clin Oncol. 2023;41(16):2060.
75. Heath JA, Campbell MA, Thomas A, Solomon B. Good clinical response to alectinib, a second generation ALK inhibitor, in refractory neuroblastoma. Pediatr Blood Cancer. 2018;65(7):e27055.
76. A study evaluating the Safety, pharmacokinetics, and efficacy of alectinib in pediatric participants with ALK fusion-positive solid or CNS tumors. ClinicalTrials.gov. 2021. NCT04774718.
77. Ceccon G, Werner JM, Dunkl V, Tscherpel C, Stoffels G, Brunn A, et al. Dabrafenib treatment in a patient with an epithelioid glioblastoma and BRAF V600E mutation. Int J Mol Sci. 2018;19(1):1090.
78. Meletath SK, Pavlick D, Brennan T, et al. Personalized treatment for a patient with a BRAF V600E mutation using dabrafenib and a tumor treatment fields device in a high-grade glioma arising from ganglioglioma. J Natl Compr Canc Netw. 2016;14(11):1345–50.

Publisher's Note